Soil-Dependent Topographic Effects: A Case Study from the 1999 Athens Earthquake

Dominic Assimaki,[a] M.EERI, Eduardo Kausel,[b] M.EERI, and George Gazetas,[c] M.EERI

In the M_s 5.9 Athens, Greece, earthquake, surprisingly heavy damage occurred on the eastern bank of the Kifissos River canyon. To explore whether the particular topographic relief and/or the local soil conditions have contributed to the observed concentration and non-uniform damage distribution within a 300-m zone from the canyon crest, we conduct finite-element analyses in one and two dimensions, using Ricker wavelets and six realistic accelerograms as excitation. The nonlinear soil response is simulated in the time-domain using a hyperbolic stress-strain model, and also approximated using a modified equivalent-linear algorithm; results obtained by means of the two methods are discussed in detail. Our simulations show that topographic effects are substantial only within about 50 m from the canyon ridge, materializing primarily because of the presence of relatively soft soil layers near the surface of the profile. We then introduce the concept of two-dimensional/one-dimensional response spectral ratio to describe the effects of topography as a function of local soil conditions, and suggest a frequency- and location-dependent topographic aggravation factor to be introduced for the modification of design spectra in a seismic code. [DOI: 10.1193/1.2068135]

INTRODUCTION

Observations have shown that topographical and geological irregularities can cause important spatial variations in the intensity and frequency content of strong ground shaking. Diffraction and focusing of the incident seismic waves can generate large amplification and reduction of ground shaking over short distances. This variability has been attributed to the earthquake source mechanics, the propagation of seismic waves from the source to the site, and the subsequent reflection, refraction and diffraction of incident waves at strongly heterogeneous near-surface soil formations. Therefore, source, path, and *site* conditions must be taken into consideration when assessing the ground motions at a given location.

Evidence from destructive earthquakes indicates that damaging effects tend to increase when steep relief or complicated topography are present. Numerous cases of recorded motions and observed earthquake damage in the recent past have identified to-

[a] Assistant Professor, Georgia Institute of Technology, School of Civil and Environmental Engineering, 790 Atlantic Drive NW, Atlanta, GA 30332
[b] Professor, Massachusetts Institute of Technology, 77 Massachusetts Avenue, Cambridge, MA 02139
[c] Professor, National Technical University of Athens, Athens, Greece

Earthquake Spectra, Volume 21, No. 4, pages 929–966, November 2005; © 2005, Earthquake Engineering Research Institute

pographic amplification as an important contributing factor. Examples include observations from the 1971 M_s 6.6 San Fernando (Boore 1972), 1980 M_s 6.9 Irpinia (Castellani et al. 1982), 1983 M_s 6.4 Coalinga (Celebi 1991), 1985 M_s 7.8 Chile (Celebi 1987), 1987 M_s 6.6 Superstition Hills (Celebi 1991), 1987 M_s 5.9 Whittier Narrows (Kawase and Aki 1990), 1994 M_s 6.7 Northridge (Ashford and Sitar 1997), and 1999 M_s 6.2 Armenia, Colombia, (Restrepo and Cowan 2000) earthquakes. As a result of these earthquakes a considerable effort has been made to model and quantify the effects of topography.

Instrumental evidence of topographic amplification is also available, for the most part from weak seismic events; for a detailed review, the reader is referred to Bard (1999). However, results from studies on weak motion data or ambient noise may not be applicable to describe topographic effects during strong ground shaking, which is usually associated with nonlinear phenomena. Among the limited evidence that exists from strong and destructive seismic shaking is the Pacoima Dam Abutment record of the 1971 San Fernando earthquake, two records in the 1985 M_s 6.2 Nahanni earthquake, and the astonishing records in the Tarzana Hill Nursery during the 1987 Whittier Narrows and the 1994 Northridge earthquakes (Boore 1973, Leeds 1992, Sanchez-Sesma 1985, Aki 1988, Shakal et al. 1994, Bouchon and Barker 1996). Nonetheless, there exist very few, if any, well-documented case studies where topographic effects are illustrated for *strong* ground motion.

The 1999 Athens earthquake offers a valuable case history demonstrating the significant role played by soil conditions and topography in amplifying the ground motion and producing differences in structural damage from place to place, even within a small town. In this paper, we consider the local site effects that were indirectly observed during the event in the community of Adàmes (located near the banks of the Kifissos River canyon), and we assess the relative importance of soil conditions and topography in modifying the input seismic motion. Our results show that the extent of topographic aggravation of surface ground motion at a given site depends on the local soil stratigraphy and heterogeneity, especially when the ground shaking is strong enough to elicit clear nonlinear effects.

EARTHQUAKE CHARACTERISTICS AND DAMAGE DISRIBUTION

The Athens, Greece, earthquake of 7 September 1999, occurred at 11:56:50.5 GMT at the western bounds of the greater metropolitan area of Athens; it was the first event ever reported to have caused casualities within the urban area of Athens, and can certainly be regarded as the worst natural disaster in the modern history of Greece.

Greece is undergoing active extension in a back-arc setting, due to the subduction of the African plate beneath the Eurasian plate at the Hellenic Arc. In regions such as the Gulf of Corinth, just a short distance from the epicenter of the Athens earthquake, damaging moderate-magnitude shocks are relatively frequent. As reported above, however, few damaging earthquakes have been documented in the epicentral region (Figure 1a), with the 1981 Gulf of Corinth earthquakes being the most recent to cause damage in Athens (Psycharis et al. 1999).

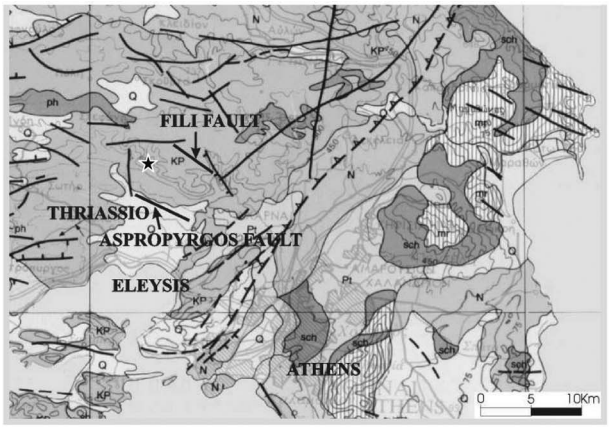

(a)

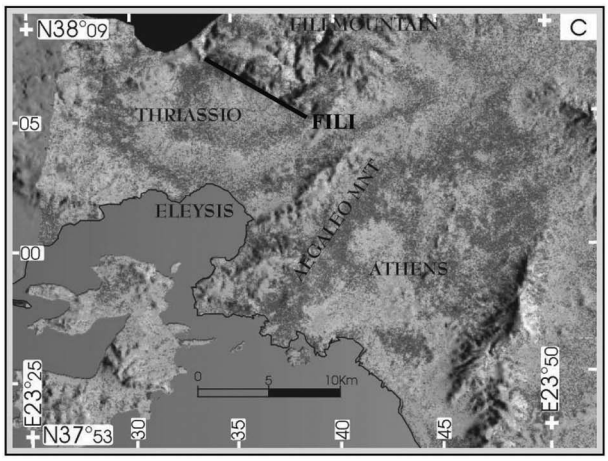

(b)

Figure 1. (a) Epicentral region with mapped faults (after Pavlides et al. 2002). The red star denotes the USGS epicenter (38.13 N, 23.55 E). *Upper NW group* consists primarily of Mesozoic carbonate rocks overlying an elastic formation of shale and sandstone. *Lower SE group* consists mainly of metamorphic rocks that crop to the east and to the south of the Athenian basin. (b) Coseismic ERS-2 satellite radar interferogram, showing the relative ground surface displacements during the period from 19 September 1998 to 9 October 1999 (after Kontoes et al. 2002).

During the main shock, no surface faulting was observed in the epicentral region. As a result, great uncertainty and confusion arose regarding the source of the event, which was finally identified as being the Fili fault (Figure 1a) based on a multidisciplinary approach that employed the following techniques: (1) field observations, mapping, and fault measurements along the three main faults of the epicentral area; (2) morphotectonic approaches supplemented by 20-m digital elevation models, (3) Landsat imagery interpretation (Figure 1b); (4) macroseismic effects evaluation; and (5) aftershock dis-

tribution data and focal mechanisms of the main shock. Additional data came from radon soil emission measurement some days after the earthquake, which are concentrated mainly along the eastern edge of the Fili fault. Detailed seismological information can be found in Stavrakakis (1999), Delibasis et al. (2000), Tselentis and Zahradnik (2000), Rondogianni et al. (2000), Kontoes et al. (2000), and Pavlides et al. (2002). The projection of the rupture on the ground surface, along with the geography of the heavily damaged region, are schematically illustrated in Figure 2a.

The modeling of teleseismic P and SH waves provided a well-constrained focal mechanism of the main shock with strike of 105° and dip of SSW55°. The rupture nucleated at 38.105° N, 23.565° E, approximately 20 km NW of the city of Athens (Figure 1), at a focal depth of 8 km. Subsequently, the rupture propagated upwards, with the number of aftershocks being greater in the eastern part of the fault, i.e., the part closer to Athens (Papadimitriou et al. 2002). One would therefore expect forward-directivity effects to have been present in the ground motions experienced at sites located to the east of the rupture zone, at distances within a few kilometers; such is indeed the site studied in this paper.[1] Finally, the rupturing process terminated beneath the Aegaleo mountain range, whose orientation is nearly perpendicular to the strike of the activated fault. The mountain seems to have acted as a barrier, and the sudden interruption and possible turning of the rupturing process would have an effect similar to an impact, generating high-acceleration high-frequency ground motions.

Despite its moderate magnitude (M_s 5.9) and focal depth (8 km) (Papadopoulos et al. 2000), the earthquake resulted in the loss of 143 lives, the collapse of about 200 residential and industrial buildings, and the severe damage of another 13,000. The geographical distribution of buildings, the collapse of which caused fatalities, is indicative of the intensity of damage in the various towns and regions; their location is depicted in Figure 2a. In the town of Adàmes studied in this paper, at a distance 8–9 km from the surface projection of the fault, the observed intensity varied in the modified Mercalli intensity (MMI) from VII^+ to IX.

The damage distribution was characterized as being strongly non-uniform, not only in the region of interest, but also in the majority of the hardest hit regions and towns. The satellite image of Figure 2b indicates the four locations where the damage intensity reached MMI IX^-.

The seismic intensities of the most severely stricken regions, as well as their closest distance from the surface of the rupture, are summarized in Table 1. The damage intensity in surrounding areas was much less, not exceeding MMI VII at nearly rocky sites (see locations (f) in Table 1). As a striking example, in the town of Menidi (at 2–5 km distance from the fault), the damage varied from a catastrophic MMI IX in the northern part of the town, to a modest MMI VII^+ south of the town center, a distance less than 1 km. Although numerous factors may have contributed to such non-uniformity, it is be-

[1] Note that whereas forward-directivity effects are well documented mostly with strike-slip and thrust fault events, evidence of their importance in normal-fault moderate-magnitude events is also available: see Gazetas et al. (1995, 1996) and Gazetas et al. (1990) regarding the 1986 M_s Kalamata earthquake and the 1995 Aegion M_s 6.2 earthquake in Greece.

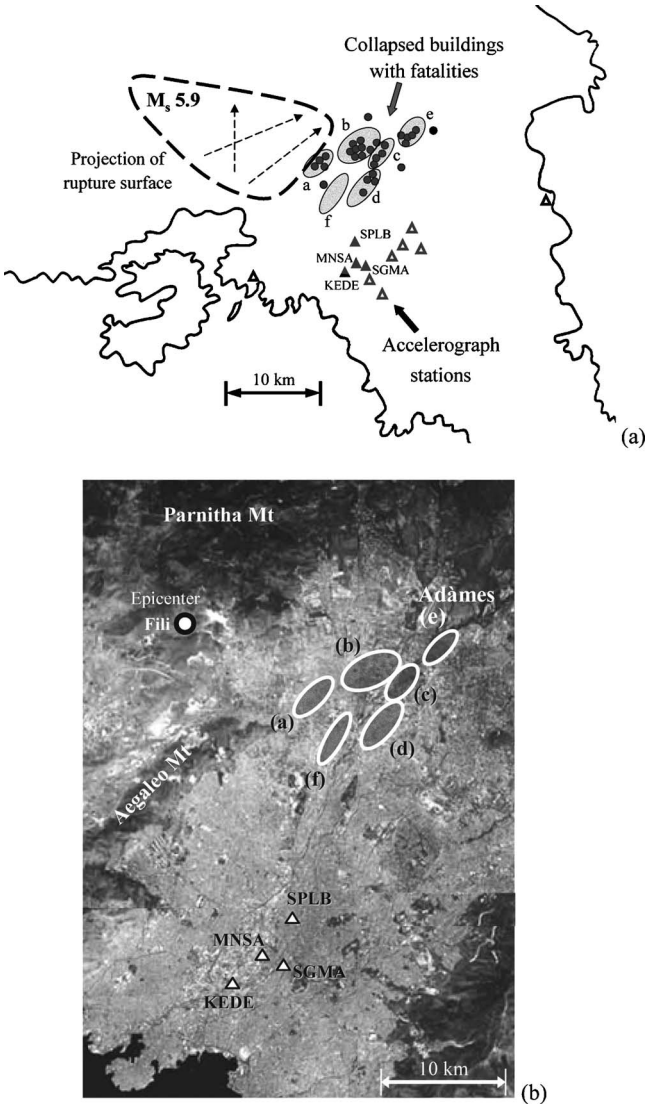

Figure 2. (a) Sketch of the map of the earthquake-stricken region, showing the surface projection of the fault. The triangles indicate the location of accelerograph stations, four of which (shown with filled triangles) are utilized in our study. The black dots show the location of the 28 collapsed buildings with human casualties. The dashed arrows illustrate schematically the direction of fault rupture. (b) Satellite image of the Athens metropolitan area, showing the areas a–f (Table 1), the four strong-motion stations, and the epicenter of the Athens 1999 main shock.

lieved that *local geotechnical and geological conditions* exerted a major influence on the ground-motion characteristics and the resulting damage patterns: (1) the local soil conditions in amplifying the seismic motion (one-dimensional), and (2) diffraction effects

Table 1. Modified Mercalli intensity in regions/towns of collapsed buildings (a–e) compared to damage in three nearby towns (f). Their location is depicted in Figure 2.

		Observed MMI		
Region	Name	Max	Min	Distance to fault (km)
(a)	Ano Liosia	IX	VII	1–3
(b)	Menidi	IX	VII	3–5
(c)	Chelidonou	IX	VII	6–7
(d)	Metamorfosis	VIII$^+$	VII$^-$	7–8
(e)	Adàmes	IX	VII	8–10
(f)	Kamatero	VIII	VII	5–6
	Petroupolis	VIII$^-$	VII	7–8
	Peristeri	VII$^+$	VII	8–10

caused by the irregular topographic relief, which further intensified the surface response (two-dimensional).

ADÀMES: OBSERVATIONS, TOPOGRAPHY, SOIL

The town of Adàmes is a community of medium to low population density (3,000 residents in an area approximately 1,200 m by 300 m), located next to the deepest canyon of the Kifissos River (the main river of the Athens metropolitan area). Built mostly in the 1970s and early 1980s, Adàmes consists mainly of two- to four-story reinforced concrete buildings.

Compared to towns located at equal or smaller distances from the source, the structural quality in Adàmes is considered to be similar (perhaps even better). Nonetheless, the intensity in many of these towns (such as Kamatero, Petroupolis, and Peristeri) did not exceed MMI VIII, and caused only two casualties in a single collapsed building. By contrast, the intensity in Adàmes reached MMI IX, and the collapse of three industrial and two residential buildings caused 18 deaths. Many other buildings either collapsed or exhibited soft-story failures, and were subsequently demolished. Their location is depicted in Figure 3. Clearly, structural damage is concentrated in two regions, namely Site 3 next to the Kifissos canyon (within one or two blocks from the crest of the cliff), and Site 2 at a distance 200–300 m from the crest. Some scattered—less intense—damage was also observed at intermediate distances (i.e., within the zone 50–200 m from the crest).

A topographic survey of the canyon produced by the Survey Engineering Department of the National Technical University in Athens (March–April 2000) produced the cross section M-M′ shown in Figure 4a. The slightly idealized geometry used in our investigation is also shown in this figure. The 40-m-deep canyon and the 30° slope inclination are also depicted in the photo of Figure 4b.

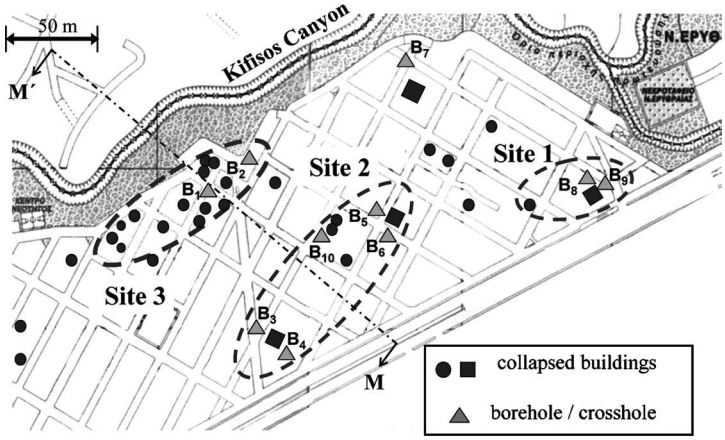

Figure 3. Plan view of Adàmes, showing the heavily damaged and collapsed residential (circles) and industrial (squares) buildings. The location of the geotechnical boreholes (B_1–B_{10}) and the topographic cross section M-M′ is also shown. Sites 1, 2, and 3 correspond to locations where the dominant soil conditions are characterized by profiles A, B, and C, respectively.

The geotechnical investigation of the area consisted of the drilling of ten boreholes with SPT measurements (N_{SPT}) and laboratory testing. Eight of these were approximately 35 m deep, and two reached almost 80 m. Some indirect evidence for greater depths was extrapolated from two 150-m-deep boreholes drilled for the under-construction Olympic Village, located 1.5 km west to northwest of Adàmes. The empirical correlation

$$V_S[\text{m/s}] = 97.0\, N_{SPT}^{0.314}, \tag{1}$$

proposed by Imai and Tonuchi (1982), was used to estimate low-strain shear-wave velocity profiles. In addition, shear-wave velocity profiles were obtained at four locations with use of the cross-hole technique. The borehole locations are shown in Figure 3.

Results emerging from this investigation are plotted in Figure 5, where three characteristic low-strain shear-wave velocity (V_S) profiles are constructed to describe the local soil conditions in Adàmes (referred to as profiles A, B, and C). The figure shows both the cross-hole V_S variation with depth and the idealized stratified profiles used in our simulations. Overall, the following observations can be made:

- All profiles are made up of alternating soil layers of silty-gravelly sands and sandy-gravelly clays to a depth of 20–30 m from the surface. Intervening layers of sandstone or marl were also found in some boreholes.
- The average velocity of the top 30 m ($V_{S,30}$) for the three sites is approximately: 500 m/sec for profile A, 400 m/sec for profile B, and 340 m/sec for profile C, indicative of very stiff (profile A), just stiff (profile B), and moderately stiff (pro-

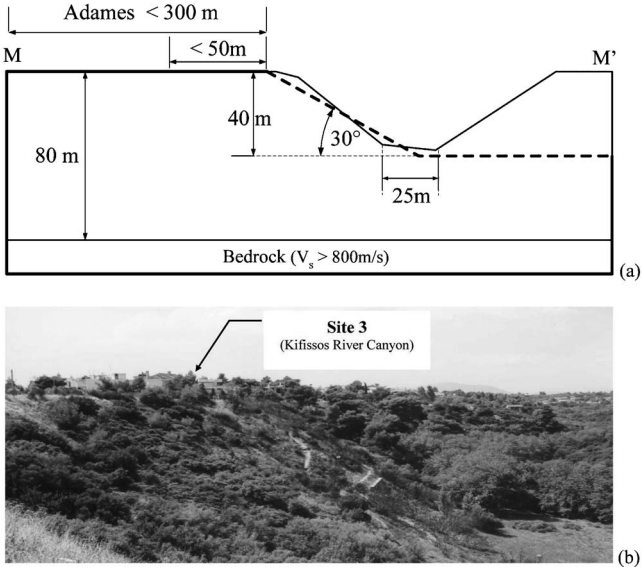

Figure 4. (a) Typical idealized cross section of the topographic relief of Kifissos River Canyon and the region of Adàmes. Site 3 is located 10–50 m behind the crest, and Site 2 approximately 300 m. The idealized geometry used in our 2-D simulations is also shown (dashed line). (b) Bird's-eye view of the cliff at Kifissos River Canyon.

file C) locations, according to the site characterization of the European Seismic Code (*EC8*) (European Comm. 2000).

- The fundamental resonant frequency (f_1) of the idealized stratified media (estimated using the weighted average shear-wave velocity of the corresponding profiles) is 1.9 Hz for Profile A, 1.5 Hz for Profile B, and 1.35 Hz for Profile C.
- Although no bedrock was found down to a depth of 80 m, the layers below 30-m depth include soft rocks (marl and sandstone) with $V_s \approx 550-800$ m/s.

STRONG-MOTION RECORDS

Fifteen strong-motion accelerograph stations were triggered by the main shock within 25 km of the Fili fault. There were no records, however, in the meizoseismal area. The peak horizontal ground accelerations (PGA) in the records obtained range from approximately 0.05 g to 0.50 g. Of the 15 records obtained, we summarize in Table 2 the four stations with the strongest PGA motions, which are shown as filled triangles in Figure 2, noting the station name, the dominant period(s) and largest PGA of the record, and the closest horizontal distance from the surface of the rupture. For a detailed investigation of the geotechnical properties and characteristics of the strong-motion accelerograms obtained at the aforementioned stations, the reader is referred to Bouckovalas et al. (2002).

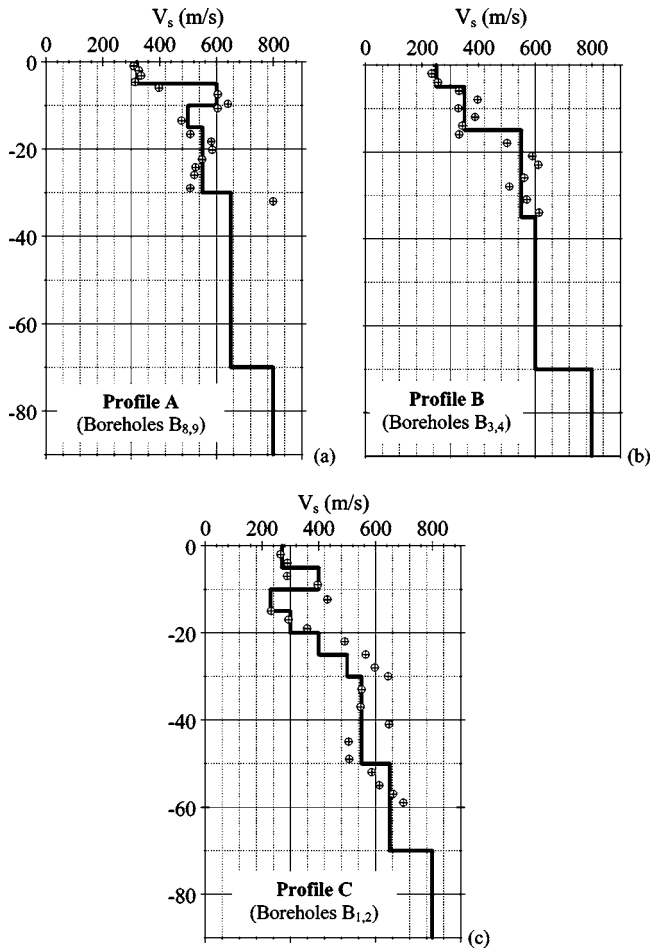

Figure 5. Shear-wave velocity variation with depth for the three characteristic soil profiles in Adàmes. The solid line corresponds to the horizontally stratified shear-wave velocity profile used in our simulations, estimated empirically from the available N_{SPT} data. The distinct values in the shear-wave velocity graphs correspond to cross-hole shear-wave velocity measured at the corresponding locations. The location of boreholes refers to the notation on Figure 3.

For the purpose of this study, we first assessed the extent to which these motions were affected by the underlying soil and by the presence of adjacent underground structures. For this purpose, we carried out one-dimensional (1-D) and two-dimensional (2-D) deconvolution analyses to recover the motion at rock-outcropping, which we then used as input motions in our simulations.

The accelerogram station Monastiraki (MNSA) recorded a very high PGA of 0.51 g in the transverse direction (MNSA record). Nonetheless, the very low dominant periods

Table 2. Accelerograph stations that recorded the strongest motions (at stations of the Geodynamic Institute and ITSAK)

Station Name	T (s)	PGA (g)	Distance (km)
MNSA	0.15, 0.08	0.51	11
SPLB	0.27, 0.14	0.36	9
KEDE	0.22	0.30	13
SGMA	0.21	0.23	13

of this record (0.08 s and 0.15 s) could only partly explain the modest damage observed in the vicinity of this station, despite the spectral accelerations exceeding 1.50 g.

However, having been recorded next to a deep shaft of a Metro station under construction, suspicion arose that the underground structure may have affected the recorded surface motion. Indeed, in addition to the shaft, two other underground structures were in close proximity to the instrument: a heavy-walled shallow tunnel of the old Metro line (18 m wide and 10 m deep) and a 5-m-deep excavation pit located between the instrument position and the shaft. The soil profile at the location of the station comprises stiff sandy clays and highly weathered rock formations down to at least 60 m depth, while the weighted average is $V_{S,30} \approx 400 \text{m/s}$ (Gazetas et al. 2002).

A finite-element simulation using ABAQUS (1998) was subsequently implemented with the recorded motion prescribed at ground surface, aiming to compute the far-field motion from the available surface record and structural layout of the Metro station. Equivalent-linear soil properties were assigned to the soil elements and vertical SV wave excitation was assumed. Results show that the recorded motion corresponds to far-field ground-surface acceleration amplitudes of PGA $\approx$0.22g, consistent with the peak values recorded at adjacent stations (KEDE 0.30 g and SGMA 0.23 g).

The KEDE and SPLB accelerograms are essentially free-field motions recorded on the surface of stiff soil deposits. The KEDE profile comprises a 10-m surface soil stratum of average $V_s \approx 320 \text{m/s} - 400 \text{m/s}$ underlain by soft rock of stiffness similar to that existing at the base of Monastiraki station. The SEPOLIA profile (location of the SPLB station) comprises a 13-m surface layer of alluvium with $V_s \approx 300 \text{m/s}$, underlain by stiffer rock. In both cases, the rock-outcrop motions were estimated by means of 1-D equivalent linear deconvolution analyses using SHAKE (Schnabel et al. 1972).

The motion at SGMA was recorded at 7-m depth inside an Athens Metro station completed shortly before the earthquake, and there are reasons to believe that the recorded motion may have been affected by the station structure. Nonetheless, the ground supporting and surrounding the station is described as slightly weathered rock, while the spectral characteristics of the recorded motion are rather similar to those of the nearby MNSA record, in the absence of soil-structure interaction effects. Hence, we shall characterize this time history as rock-outcrop motion.

The above four rock-outcrop accelerograms were used as input excitation in our simulations, in view of their roughly similar distances from the surface projection of the fault. Nonetheless, these four motions were recorded within a narrow region located 10 km away from the end of the ruptured zone, in a direction *perpendicular* to the rupture, while the studied areas (a–e), and especially Adàmes (e), lie in the direction of the fault rupture (refer to Figure 2).

There is, therefore, strong indication that *forward rupture directivity* is likely to have affected the ground motions in these areas (a–e). To account for forward-directivity effects in our study, we included two accelerograms from the 1966 M_L 5.6 Parkfield, California, earthquake in our simulations. They were recorded on soft rock at Cholame Shandon No. 8 and Temblor stations (Leeds 1992), and encompass simple long-period pulses of strong motion with relatively short duration, indicative of near-fault effects. These two records, both having a PGA of about 0.27 g, resemble the four rock-outcrop motions from the 1999 Athens event, in the time domain as well as in the frequency domain.

Accounting for the general strong-motion characteristics of the earthquake by means of the strong-motion records, as well as for directivity effects, we believe that the ensemble of these six motions offers a realistic (and perhaps almost complete) description of the free-field base motion for Adàmes. The acceleration time histories and the corresponding response spectra for 5% structural damping are shown in Figure 6.

NONLINEAR SITE RESPONSE ANALYSIS

A large number of analytical and numerical studies have provided supporting evidence of the significance of topographic effects; methods of analysis and review summaries can be found in Wong and Trifunac (1974), Bard (1982, 1995), Bard and Tucker (1985), Aki (1988), Sanchez-Sesma and Campillo (1991), Sanchez-Sesma (1999), Faccioli (1991), and Finn (1991). Nonetheless, as shown by Geli et al. (1988), the simultaneous effect of soil heterogeneity (both vertical as well as lateral) may also be significant, although not so well documented. Ashford et al. (1997), who studied topography effects for steep slopes by decoupling the amplification caused by topography from that caused by soil stratigraphy, showed that topography effects can in some cases be negligible compared to the amplification that occurs in the far-field, due to soil resonance.

The response of the Kifissos canyon during the Athens earthquake offers such documented evidence of combined topography and soil effects; based on the local site conditions in Adàmes, we first assess the relative importance of soil and topography effects in modifying the intensity and the frequency characteristics of ground shaking. We then evaluate the intensity of topographic aggravation[2] phenomena as a function of local soil conditions for strong ground motion.

For this purpose, we normalize the peak time-domain and spectral amplitude of motion in the vicinity of the crest by the corresponding quantities at the far field behind the

[2] The term *aggravation* is used here to indicate the ground-motion amplification that occurs in excess of the bedrock-to-surface 1-D amplification.

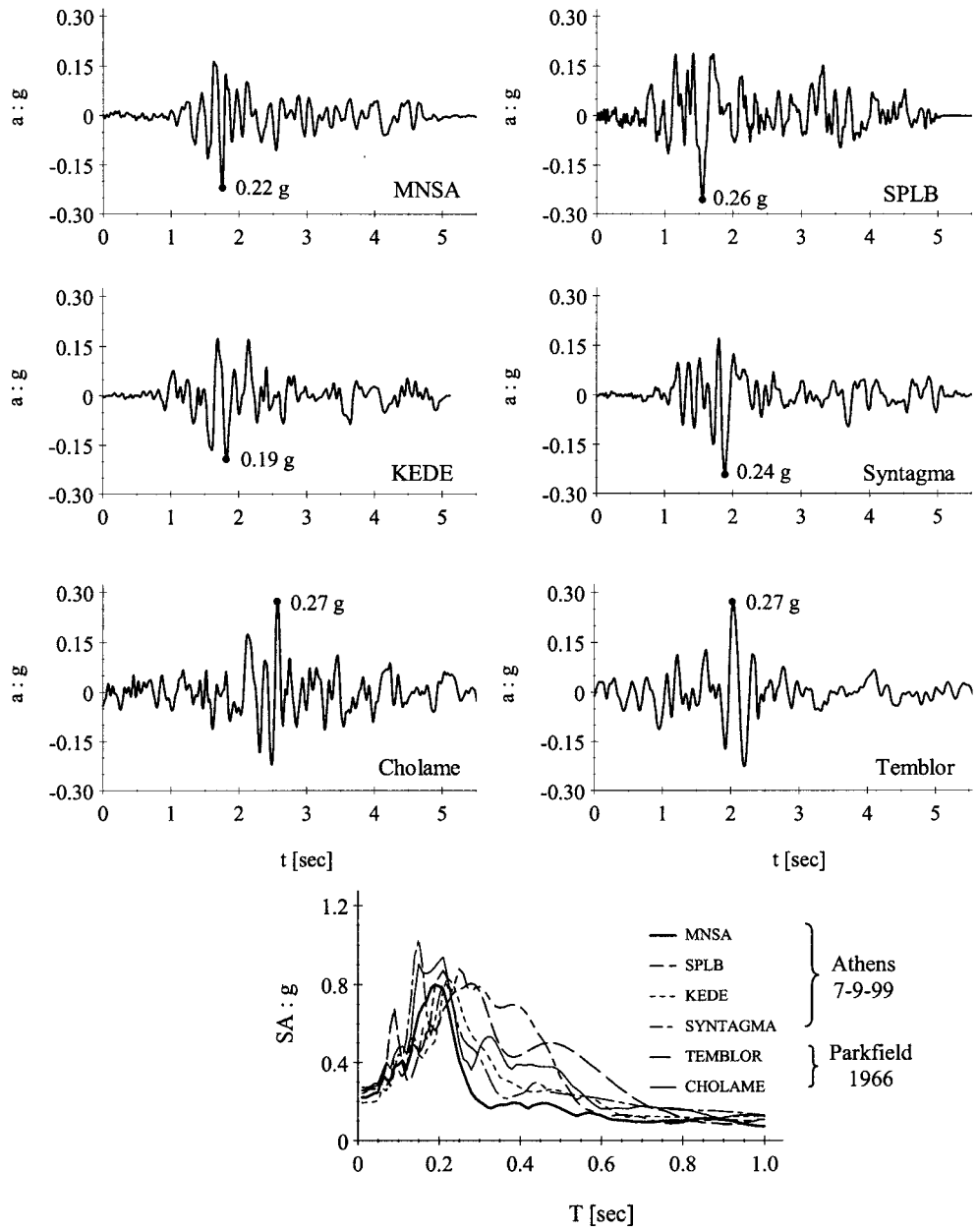

Figure 6. Rock-outcrop SV acceleration time histories and acceleration response spectra of the seismic input motions, used in our 2-D numerical simulations. For the four strong-motion records of the 1999 Athens event, the rock-outcrop time histories shown were computed using 1-D or 2-D deconvolution of the corresponding surface records.

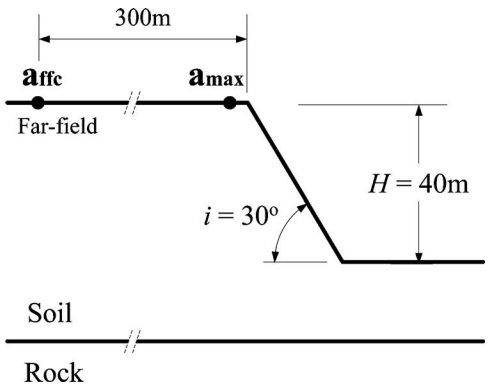

Figure 7. Definition of dimensions and symbols for the study of cliff topographic effects, with the far field defined at distance x=300m behind the crest for the purpose of this study.

crest (denoted as a_{max} and a_{ffc} in Figure 7). The far field is here defined at distance x =300m behind the canyon crest, where our preliminary investigations showed negligible topography effects for the case of vertically incident SV-waves.

Based on the amplitude of seismic excitation used in our simulations, high enough to elicit nonlinear response of the near-surface soil layers, we conduct equivalent linear and nonlinear wave propagation analyses in one and two dimensions. First, we approximate the hysteretic soil response using the equivalent linear method, modified to account for the effects of confining pressure and the frequency-dependent amplitude of the strains elicited in the soil by the seismic motion. With this modification, we avoid the artificial suppression of high-frequency/low-amplitude components of seismic motion of the standard algorithm. For further details, the reader is referred to Kausel and Assimaki (2001) and Assimaki and Kausel (2002).

Next we perform incremental nonlinear analyses using the hyperbolic stress-strain model in Equation 2, originally proposed by Hardin and Drnevich (1972) and modified by Hayashi et al. (1992):

$$\frac{\tau}{G_0 \gamma_r} = e^{-ax} f\left(\frac{\gamma}{\gamma_r}, n_L\right) + (1 - e^{-ax}) f\left(\frac{\gamma}{\gamma_r}, n_u\right) \tag{2a}$$

$$f\left(\frac{\gamma}{\gamma_r}, n\right) = \frac{\left(\frac{2}{n}\frac{\gamma}{\gamma_r} + 1\right)^n - 1}{\left(\frac{2}{n}\frac{\gamma}{\gamma_r} + 1\right)^n + 1}, \quad n > 0 \tag{2b}$$

where τ is the shear stress,

γ is the shear strain,

$\gamma_r = \tau_{max}/G_0$ is a reference strain,

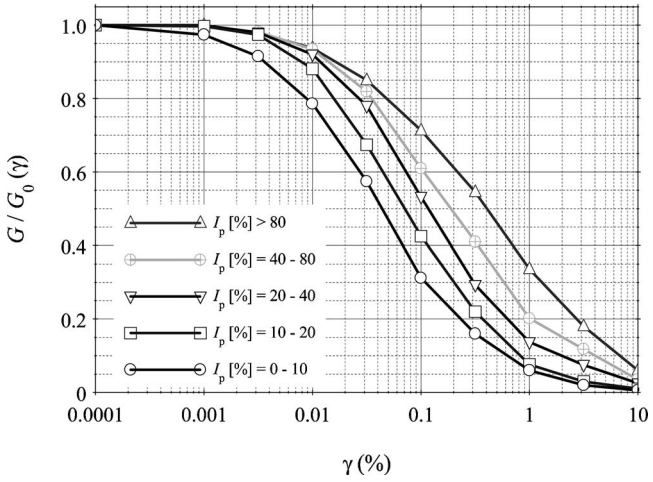

Figure 8. Shear modulus degradation curves, defined as a function of the plasticity index I_p (after Vucetic and Dobry 1991).

τ_{max} is the maximum shear-stress at failure,
n_L and n_u are used to fit the experimental stress-strain curve at small and large strain levels, respectively, and a controls the transition zone between the two strain levels with increasing γ.

For the time-domain nonlinear simulations, we use the finite-element code DYNAFLOW (Prévost 1995), where the modified hyperbolic stress-strain model was already implemented.

The shear modulus degradation and damping curves for cohesive materials of Vucetic and Dobry (1991), were used for our equivalent-linear simulations; for each soil layer, the dynamic soil properties were selected on the basis of the plasticity index laboratory results in Adàmes (Figure 8). For consistency, the hyperbolic (nonlinear) model parameters were calibrated to reproduce the published dynamic shear soil behavior.

ONE-DIMENSIONAL SOIL AMPLIFICATION

We first investigate the effects of local soil conditions at the Kifissos ravine site, by performing nonlinear, 1-D wave propagation analyses for the far-field conditions beyond the crest. Figure 9 shows the strain-compatible soil properties for profiles A, B, and C. For each stratified medium, the variation with depth corresponds to the mean value of the last linear iteration, performed for the six strong-motion records. We have also assessed the nonlinear soil response through the variation of minimum secant shear modulus with depth, extracted from the largest hysteresis loop of the nonlinear solution.

Results show that the frequency content of seismic input motion—in addition to the peak amplitude—plays a very important role in the extent of nonlinearity exerted by the soil profile. In the ensuing, we illustrate the differences in ground surface response that

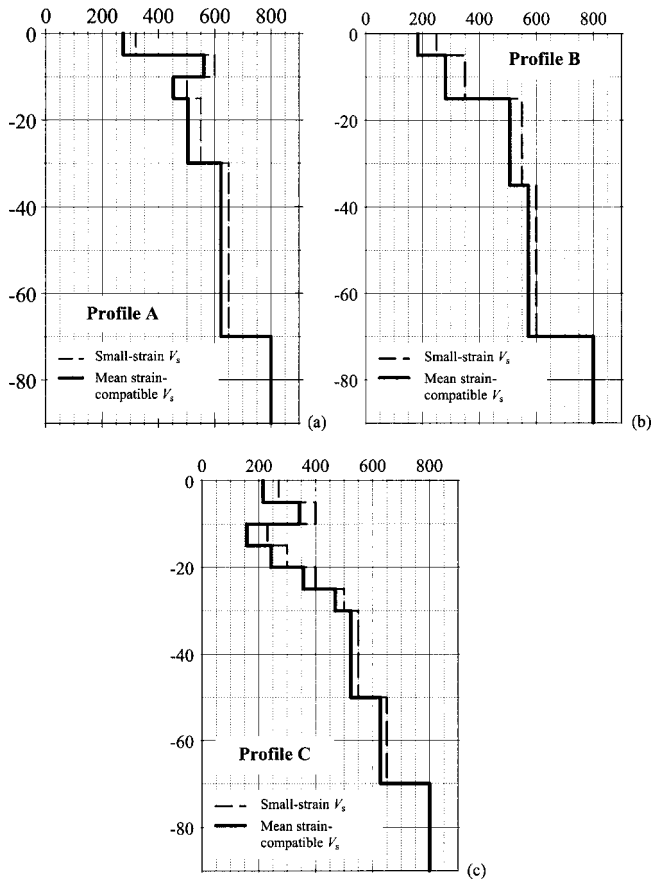

Figure 9. Small-strain (dashed line) and mean 1-D strain-compatible shear-wave velocity (solid line) corresponding to the last iteration of the equivalent linear approach for the three typical soil profiles in Adàmes.

result from (1) near-field motions (such as Cholame), characterized by long-period and high-amplitude pulses, which are shown to affect the material response down to a rather significant depth; and (2) more distant seismic events (such as MNSA), relatively rich in high frequencies due to scattering, shown to result in nonlinear response of the uppermost soil layers only.

Typical simulations for the three profiles are illustrated in Figure 10a, where acceleration time histories of ground surface motions obtained by means of the two methods are compared, for two typical input motions, namely the Cholame and the MNSA record. As can readily be seen, results are found to be in very good agreement in terms of peak amplitude and frequency content of the predicted surface response. Nonetheless, the *true* nonlinear surface response was found to be artificially rich in high-frequency ($>$15Hz) components, attributed to numerical instabilities and successively filtered us-

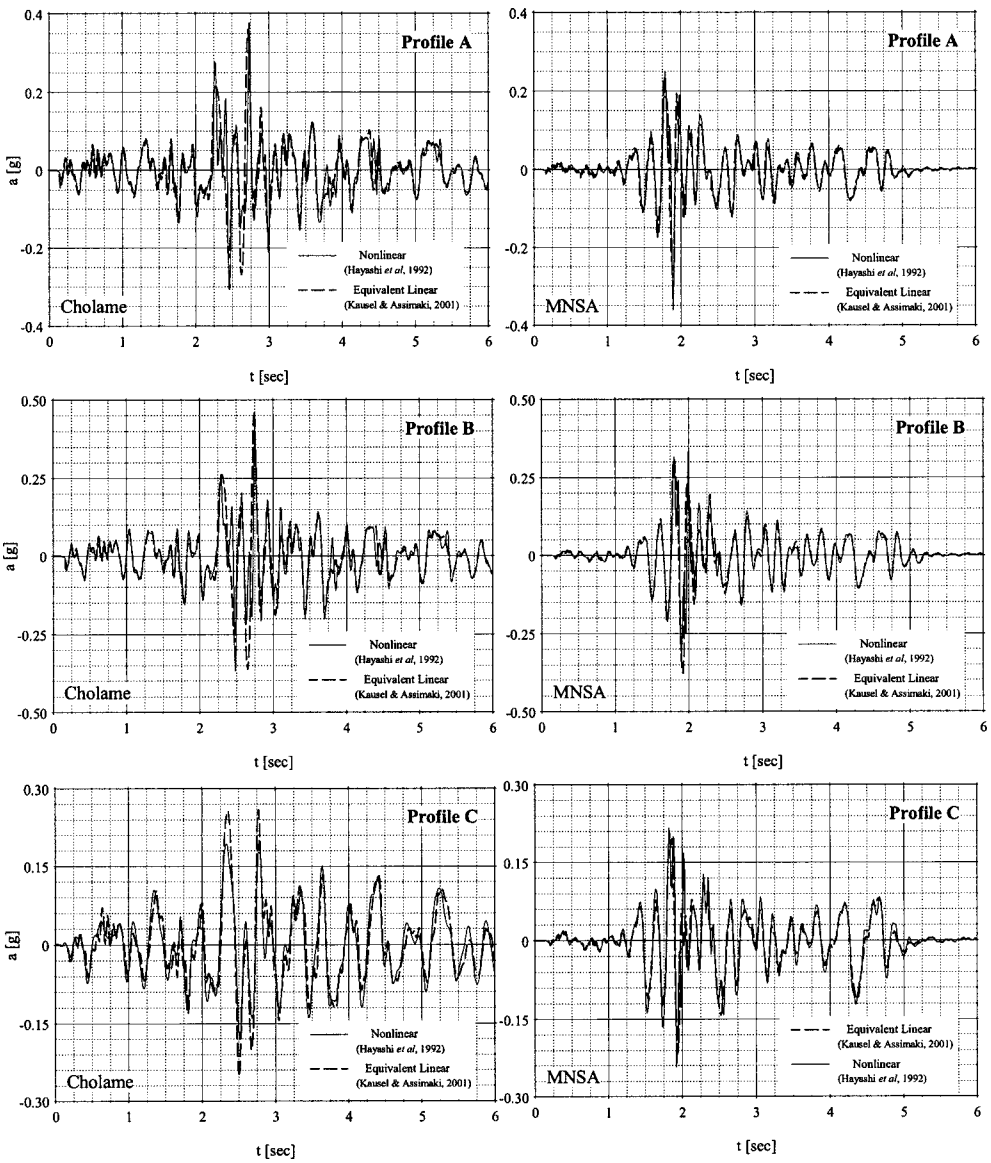

Figure 10a. Surface response of profiles A, B, and C subjected to rock outcrop motion of two typical acceleration time histories: comparison of equivalent linear (dashed line) and filtered nonlinear (solid line) response with consistent shear modulus degradation curves.

ing the Butterworth or maximally flat amplitude filter. It should be also noted that the observed consistency of the two solutions in terms of surface ground motion does not necessarily imply identical variation of strain-compatible dynamic soil properties with depth.

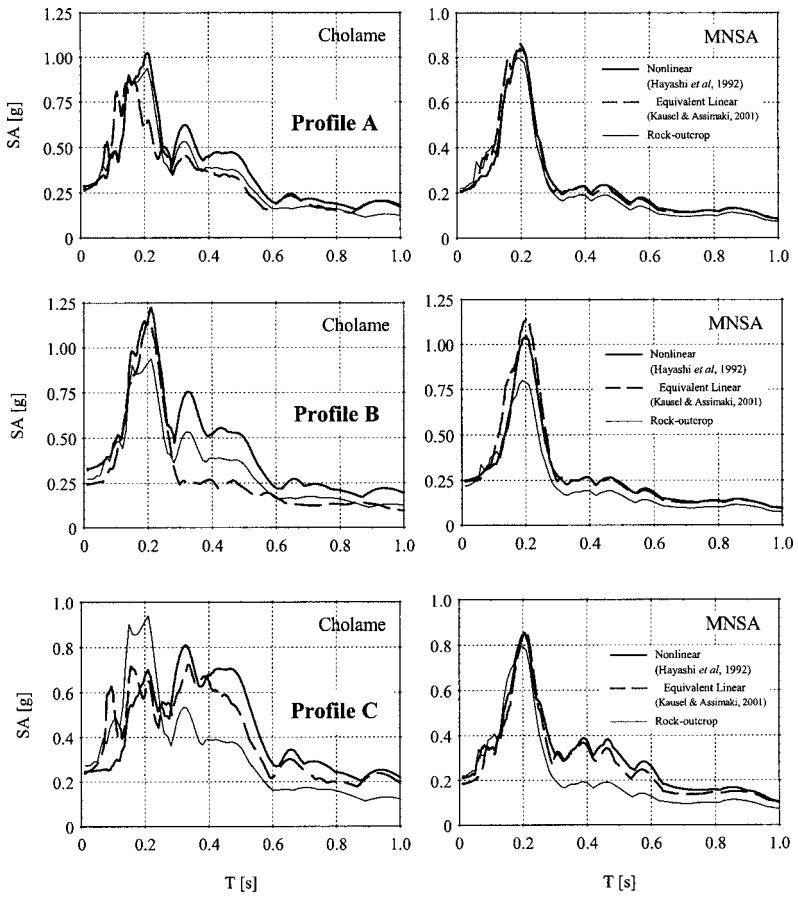

Figure 10b. Far-field surface response spectra of profiles A, B, and C subjected to seismic rock outcrop motion: comparison of 1-D equivalent linear (dashed line) and filtered nonlinear (solid line) response with consistent shear modulus degradation curves; the response spectrum of the corresponding input rock-outcrop motion (light solid line) is also shown.

The main conclusions of our study on local soil effects are summarized below (see also Figure 10b). For further information, the reader is referred to Gazetas et al. (2002) and Assimaki and Gazetas (2004).

- Profile A (where the Fourlis industrial building collapsed, killing eight), being the stiffest of the three sites, shows an appreciable degree of amplification in the period range of $T < 0.30$s, where both PGA and spectral acceleration (SA) values increase by an average of about 25% compared to the rock-outcrop input motion; soil amplification becomes insignificant at higher periods, with the exception of the Temblor and SPLB excitations, which are rich in relatively high-period components. For these records, the fundamental *strain-compatible* period of the pro-

file (denoted here as T_{soil1}) is estimated to be $T_{soil1}=0.47$s (using the reduced shear modulus of the last iteration of the equivalent linear method, averaged over all input motions). On the other hand, the period beyond which soil amplification can be considered negligible, increases to almost $T\approx 0.50$s; this would play an important role in the response of three- to five-story buildings. Nonetheless, predicted soil amplification levels do not suffice to explain the damage intensity observed at this site.

- Profile B (where the industrial buildings Faran and Prokos and two residential buildings collapsed, causing fatalities) is softer than Profile A, and our simulations show relatively larger amplification over a wider period range. Computed PGA values are in the range of 0.30 g to 0.40 g, and the highest SA reaches 1.50 g at $T\approx 0.2$ seconds. Evidently, there is a pseudo-resonance condition at this period: the fundamental period of the soil column (estimated $T_{soil1}\approx 0.2$ sec from the surface/rock outcrop transfer function) nearly coincides with the dominant excitation period (denoted here as $T_{excit.}$), $T_{excit.}\approx 0.20$ s.
- Profile C (where several residential buildings collapsed) is the softest of the three sites. The fundamental natural period of the soil deposit in the last step of the iterative algorithm is estimated to be $T_{soil1}\approx 0.72$ sec, while most of the rock-outcrop excitations have much lower dominant periods, $T_{excit.}\approx 0.10-0.20$ sec. Hence no enhancement or even deamplification is expected in PGA and SA values due to local soil conditions for periods $T<0.25$ sec, a fact that was confirmed through our 1-D simulations. On the other hand, components of the seismic input in the approximate period range of $T=0.30$s to 0.60s, are shown to almost double in amplitude; this, however, can have substantial effects only for relatively high-period incident motions. Figure 10b illustrates the response of profile C to the MNSA ($T_{excit.}=0.23$s) and Cholame ($T_{excit.}=0.43$s) records; while no amplification occurs for the high-frequency former record, the high-period components of the latter are indeed enhanced.

It should be noted that the Cholame input motion is illustrated herein in the absence of records from the Athens 1999 event that imprint forward-directivity effects, whereas strong evidence suggests that they must have been present in the motion experienced by the town of Adàmes (Stavrakakis 1999, Delibasis et al. 2000, Tselentis and Zahradnik 2000, Rondogianni et al. 2000, Papadopoulos et al. 2000, Papadimitriou et al. 2002). The rock-outcrop MNSA motion represents a narrow-band, high-frequency motion, with maximum spectral acceleration value that coincides with the linear fundamental frequency of profile B, resulting in resonance phenomena.

Qualitative comparison of the predicted ground surface accelerations with the observed intensity of structural damage in Adàmes, leads to the following conclusions:

- For profile B, 1-D amplification of motion is substantially strong, and thus compatible with the observed high intensity of damage in that region, similar in the far field and next to the canyon crest.

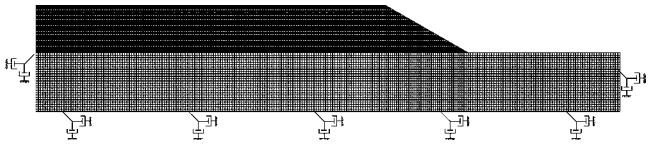

Figure 11. Schematic representation of the 2-D finite-element model used in the simulations, indicating the presence of absorbing elements at the base and lateral boundaries.

- For profiles A and C, soil effects alone do not suffice to explain the observations. This is particularly evident for the stratigraphy of profile C, characteristic of one of the most heavily damaged regions during Athens earthquake, where deamplification of the incident motion due to soil softening is predicted for the period range that coincides with the fundamental period of typical local structures.

Our 1-D simulations illustrate that simplified models can provide valuable insight towards understanding the characteristics of surface ground motion at a given site. Nonetheless, a complete site response analysis for strong ground motion should also account for the 2-D nature of the topographic feature, by simulating the interaction between irregular surface topographic features and incident seismic waves, and reproducing the diffracted wave field in the vicinity of the crest. These phenomena are believed to have played major role in the response of the Kifissos ravine.

TWO-DIMENSIONAL SIMULATIONS

We next perform 2-D finite-element simulations using the computer code DYNAFLOW (Prévost 1995), both with equivalent linear and nonlinear dynamic soil properties. The numerical model consists of plane 4-node quadrilateral and 3-node triangular finite elements, the size of which were selected on the basis of the frequency content of strong-motion records and the 1-D strain-compatible dynamic soil properties, to ensure detailed representation of the propagating wavelengths. Absorbing elements are placed around the discretized domain to avoid spurious reflections into the soil island, and the input motion is prescribed in the form of effective forcing functions at the boundary nodes, to allow for scattered waves impinging onto the boundaries to be absorbed. A schematic representation of the numerical model used in our investigation is shown in Figure 11.

For the equivalent-linear 2-D simulations, we assign strain-compatible soil properties at the end of each iteration on the basis of the root-mean-square strain exerted by each finite element (Lysmer et al. 1975):

$$\gamma_{eff} = 0.65\sqrt{\mathrm{RMS}^2(\varepsilon_x - \varepsilon_z) + \mathrm{RMS}^2(\gamma_{xz})} \cdot \frac{\max|\mathrm{a}(t)|}{\mathrm{RMS(a)}} \tag{3}$$

where ε_x and ε_z are the normal strain in the horizontal and vertical direction, γ_{xz} is the shear strain, $\mathrm{a}(t)$ is the input acceleration time history, and RMS is the root-mean-square of the time history considered. For the nonlinear incremental analyses, gravitational

loads are equilibrated by constant point loads at the base and lateral boundaries of the simulated domain and the effective forces in the far field are extracted from the 1-D nonlinear response. Note that the distance between the scatterer and the far field, and the relatively high intensity of the incident seismic motion, allows sufficient attenuation of the diffracted wavefield and results in negligible reflections from the boundaries of the numerical model.

To quantify the effects of topography as a function of local soil conditions, results are shown normalized by the corresponding far-field surface response. Note that the equivalent-linear and nonlinear solutions yield very similar surface ground motions for 1-D conditions. Therefore, comparison of the normalized surface response can also illustrate the applicability of the equivalent-linear approximation for 2-D nonlinear wave propagation problems.

HORIZONTAL STRATIGRAPHY

The shear-wave velocity distribution of the horizontally stratified profiles A, B, and C is schematically illustrated in Figure 12. The three configurations are first used to describe the spatial distribution of dynamic soil properties. Due to lack of geotechnical investigation data for locations in front of the cliff toe, soil layers at depth below 40 m behind the crest are assumed to also extend forward. Nonetheless, our preliminary investigation shows that topographic aggravation at the crest arises mainly from diffracted waves generated at the toe of the cliff and propagating upwards, which are primarily affected by the stratigraphy of the far-field soil column behind the crest. This simplification is therefore believed to have minor effects on the estimated surface response of the configuration.

Snapshots of total acceleration vectors and seismogram synthetics obtained throughout our simulations indicate that the wavefield in the vicinity of the crest results from the superposition of

(1) Direct SV waves, which arrive simultaneously at all locations of the upper and lower level surface of the configuration, since the seismic input comprises vertically incident SV-waves.

(2) Forward-scattered Rayleigh waves generated at the lower corner of the cliff, propagating along the cliff and being forced to change direction at the upper corner.

(3) Surface waves (SP), which are generated along the cliff and propagate upwards approximately with the P-wave velocity. As a result, these waves arrive behind the crest almost simultaneously with the direct SV-wave. This phenomenon is attributed to the particular geometry of the ravine, whose slope inclination nearly coincides with the critical angle for the typical Poisson's ratio ν=0.35 that characterizes sandy/clayey soils above the water table.

$$\theta_{cr} = \arcsin(V_s/V_p) = 28.71^\circ \approx i = 30^\circ \tag{4}$$

Therefore, vertically propagating waves strike the free surface of the slope virtually at critical incidence and are thus transformed into surface waves that travel along the

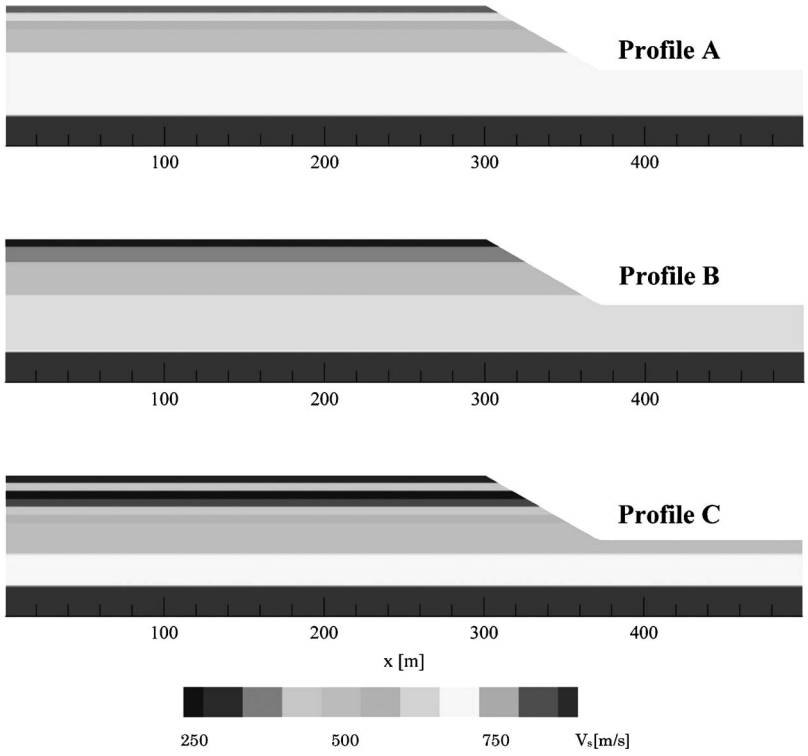

Figure 12. Two-dimensional shear-wave velocity distribution with depth corresponding to profiles A, B, and C for the horizontally stratified approximation of local soil conditions.

slope and interfere constructively with direct SV and Rayleigh waves behind the crest. As a result, substantial vertical acceleration components are generated despite the fact that the input and far field motions consist only of horizontally polarized particle motions. This component, referred to in the following as *parasitic* to emphasize its diffraction-generated nature, carries a significant portion of the seismic wave energy.

Typical time-domain results are summarized in Figure 13, for the three profiles and the ensemble of strong input motions. More specifically, Figures 13a and 13b plot the mean spatial distribution and standard deviation of normalized peak horizontal and vertical acceleration, respectively.

The spectral characteristics of the computed surface response are summarized in Figure 14. For the case illustrated in Figure 14a, the configurations are subjected to the MNSA input motion. The response spectra plotted for each profile correspond to (1) the seismic excitation (rock-outcrop motion), (2) the 1-D (far-field) surface motion, which only embodies 1-D *soil amplification* effects, and (3) the 2-D surface motion at distance $x=20.0$m behind the crest, which reflects both *soil flexibility* and *cliff topography* effects.

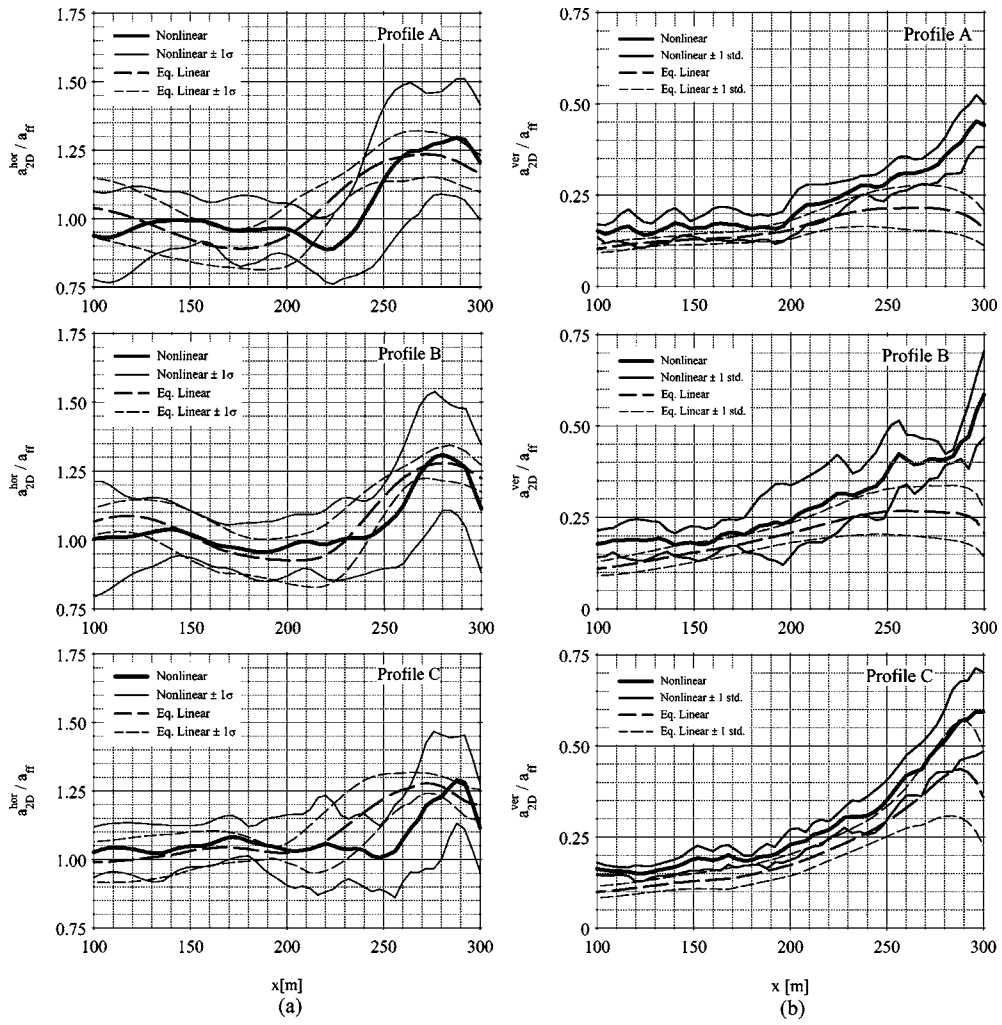

Figure 13. (a) Spatial distribution (mean and standard deviation) of normalized horizontal acceleration (with respect to the far-field horizontal surface response a_{ff}) at ground surface of Profiles A, B, and C for all six rock-outcrop seismic inputs: comparison of 2-D equivalent-linear (dashed line) and nonlinear solutions (solid line). (b) Spatial distribution (mean and standard deviation) of normalized vertical parasitic acceleration (with respect to the far-field horizontal surface response a_{ff}) at ground surface of profiles A, B, and C for all six rock-outcrop seismic inputs: nonlinear solution (solid line).

The 2-D to 1-D spectral ratio from each graph offers a measure of the topographic aggravation, which we refer to as the Topographic Aggravation Factor (*TAF*). Its mean spectrum is successively illustrated in Figure 14b for all three profiles and all six input motions. Results are shown for the equivalent linear and nonlinear response, and com-

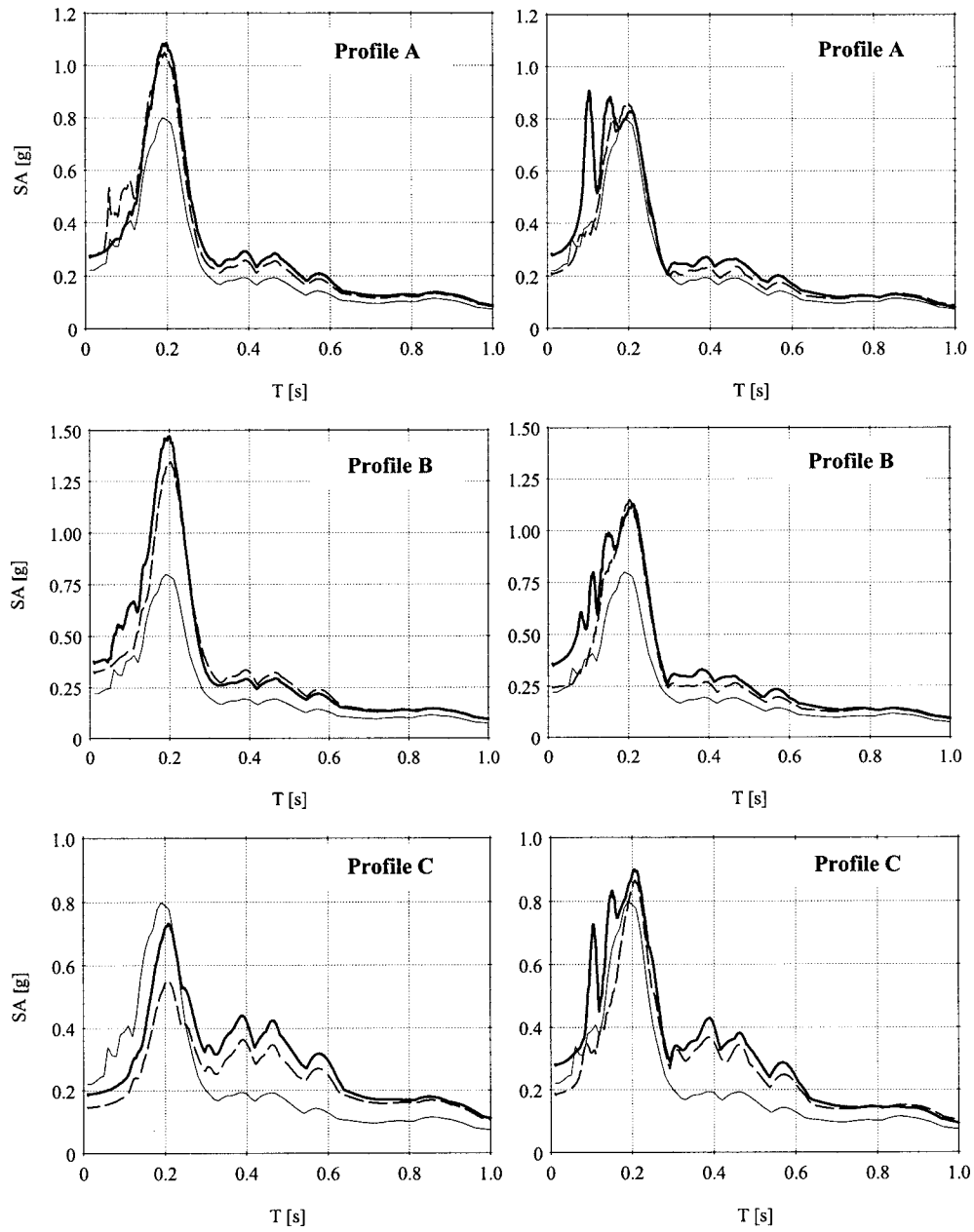

Figure 14a. Surface response spectra of profiles A, B, and C subjected to the MNSA rock outcrop motion (light solid line) corresponding to the far field (dashed line) and 2-D response (solid line) defined at location x=20.0m behind the crest): equivalent linear solution (left) and nonlinear solution (right).

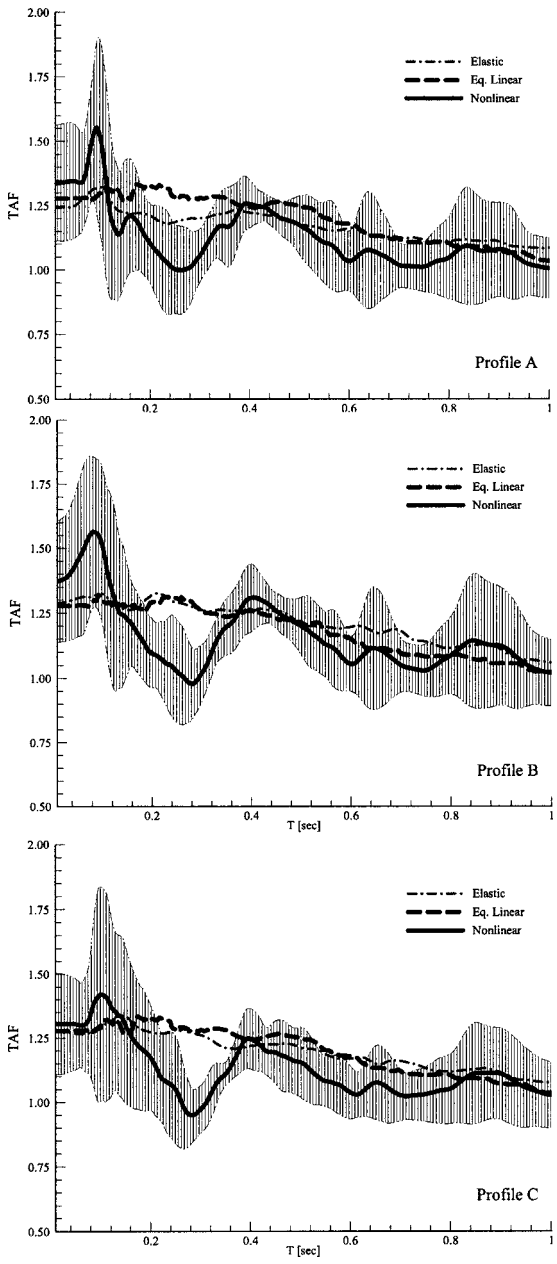

Figure 14b. Mean and standard deviation for the Topographic Aggravation Factor computed from the ensemble of 2-D nonlinear seismic wave propagation simulations for profiles A, B, and C at distance x=20m from the crest. Mean distribution of the elastic and equivalent linear analyses is also shown for comparison.

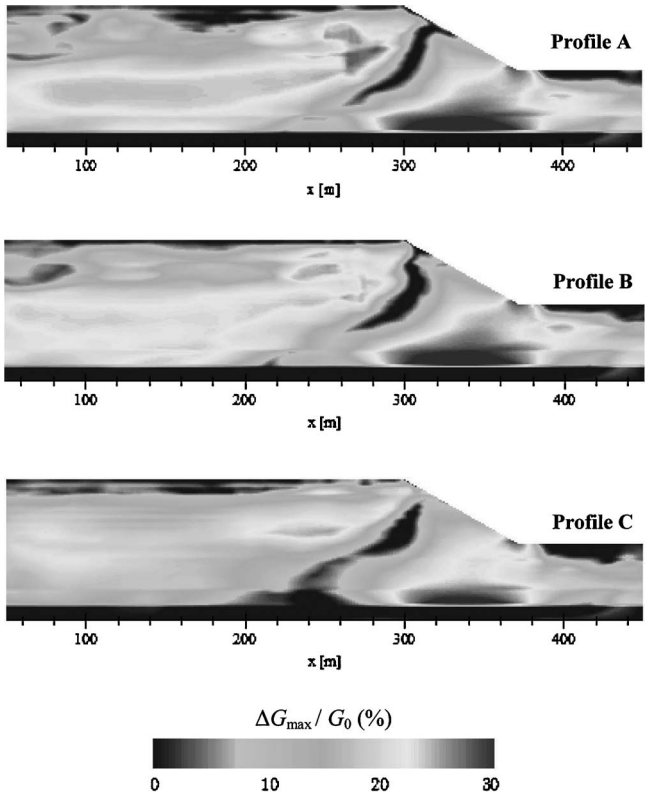

Figure 15. Percentage of shear modulus reduction (extracted from the lowest secant modulus of shear stress-strain hysteresis loop) for the Cholame rock-outcrop motion (profiles A, B, and C).

pared to the elastic solution that corresponds to the first iteration of the equivalent linear method, using the low-strain dynamic soil properties illustrated in Figure 9.

Finally Figure 15 plots the spatial distribution of maximum secant shear modulus reduction (computed at the centroid of each finite element from the largest shear stress-strain hysteresis loop) for the three profiles subjected to the Cholame seismic motion. Note that at each time step of the nonlinear solution, material strain-softening is defined according to the instantaneous shear strain level, which is not restricted in the horizontal direction due to the wavefield complexity. As a result, the response of a horizontally stratified profile to strong ground motion can be described by a strain-compatible random medium, with time-dependent stochastic properties (i.e., correlation distance, probability distribution function). Multiple scattering, reflections and refractions of wavelengths comparable to the average correlation distance of the random medium, results in excess aggravation of motion and justifies the higher frequency content of the nonlinear solution. Results of our investigation can be summarized as follows:

Table 3. Comparison of the equivalent linear and nonlinear solution, in terms of the mean value of peak normalized vertical acceleration for the ensemble of our simulations

$a_{vert}^{max}/a_{ff}^{max}$	Equivalent Linear	Nonlinear
Profile A	0.30	0.50
Profile B	0.30	0.55
Profile C	0.50	0.70

- Both nonlinear and equivalent linear analyses produce similar values of peak normalized horizontal acceleration. Profile B, which produced the highest 1-D motion amplification, also shows the largest mean topographic aggravation potential of approximately 30%. For profiles A and C, mean topographic aggravation of 25% is predicted in the frequency region of the far-field fundamental frequency.
- The predicted spatial distribution of normalized horizontal acceleration is significantly more erratic when the nonlinear approach is employed. The variability in this case is attributed to the incremental change of soil stiffness and subsequent altering of the wavefield direction; by contrast, iterations in the equivalent linear approach involve strain-compatible properties, which are retained constant throughout the analysis. Nonetheless, the zone behind the crest where 2-D aggravation phenomena are observed is, on average, of the same width in both solutions, and approximately equal to the width of the topographic feature.
- The two methods deviate significantly in terms of the predicted magnitude of *parasitic* vertical acceleration (Table 3). The observed incompatibility is again attributed to the inability of the equivalent-linear method to capture the instantaneous strain softening of the material and consequent adjustment of the seismic wavefield throughout the simulation.
- The frequency content of nonlinear surface response, illustrated by means of the *TAF*, shows substantially higher aggravation of the low-period components ($T < 0.1$s). These components correspond to average wavelengths on the order of the strain-compatible randomness of soil stiffness. In fact, it is in the high-frequency regime that theoretical elastic models fail to reproduce field-measured amplification levels. Since material softening occurs in this case as a result of a multidirectional wavefield, short-wavelength, low-amplitude components that are not subjected to intrinsic attenuation are trapped in the near-surface between patches of material, which undergoes spatially varying shear degradation, and is further amplified. Furthermore, the elastic finite-element solution was shown to be sensitive in the correct selection of Rayleigh damping coefficients; when calibrated for the mean frequency of input motion, the solution artificially attenuates the high-frequency components.

- The spectrum of *TAF* shows that topography effects are negligible in the period range $0.2\text{s} < \text{T} < 0.4\text{s}$ for the particular geometry, where no 1-D amplification occurs for the particular profile. They become important again in the period range of the so-called topographic frequency $0.4\text{s} < \text{T} < 0.6\text{s}$ (see Ashford et al., 1997), defined as a function of the location of maximum motion aggravation behind the crest; for a stratified soil configuration, this can be approximated by $5H/\bar{V}_s$ (H is the height of the feature and $\bar{V}_s$ is the mean shear-wave velocity of the far field).

LATERAL HETEROGENEITY

Aggravation of high-frequency components becomes more pronounced when we introduce small-strain material randomness to investigate the effects of simultaneous scattering of seismic energy propagating through a heterogeneous nonlinear medium with irregular surface topography. Our elastic parametric simulations have shown that the spatial variability of material properties favors the enhancement of frequency components whose wavelengths are comparable with the correlation distance of the random medium. By contrast, phenomenological attenuation was observed for lower frequencies, attributed to diffusion of the propagating energy and consequent reduction of focusing at the vertex (Assimaki 2004).

Recall that when interpreting the nonlinear material behavior as instantaneous heterogeneity due to material softening (strain-compatible stiffness), the same phenomenon was observed, namely enhancement of high-frequency components of motion. In this case, however, spatial variability of soil properties is initiated as a result of seismic energy focusing at the crest, and therefore attenuation due to scattering is not observed.

To evaluate the net effects of small-strain and strain-compatible heterogeneity, we perform Monte Carlo simulations based on the methodology introduced by Popescu (1995), which combines Gaussian stochastic vector fields of the small-strain V_s with deterministic nonlinear finite-element analyses. The limited amount of available field data from the Kifissos ravine site was first combined with the statistical properties of an adjacent cohesive site for the estimation of the spectral density and marginal probability distribution functions. Accounting for sediment formation mechanisms, separable correlation structures were used in the horizontal and vertical direction, with correlation distance $\theta_x = 16\text{m}$ and $\theta_z = 2.6\text{m}$, respectively. Then univariate, 2-D stochastic fields were digitally generated using the spectral representation method (Shinozuka and Deodatis 1996). Finally, a mapping technique was employed to transform the standardized sample fields to the deterministic finite-element mesh. For more details on the geostatistical analysis, the reader is referred to Assimaki (2004) and Assimaki et al. (2003).

Forty standardized sample fields were generated to describe the spatial variability of local shear-wave velocity, and each of the stratified profiles A, B, and C were used in the denormalization process to represent the mean (background) stiffness distribution. In addition, a constant standard deviation with depth ($0.15\bar{V}_s$) was employed; note that the stiffness deviation is thus reducing with depth, a typical characteristic of sedimentary soil profiles.

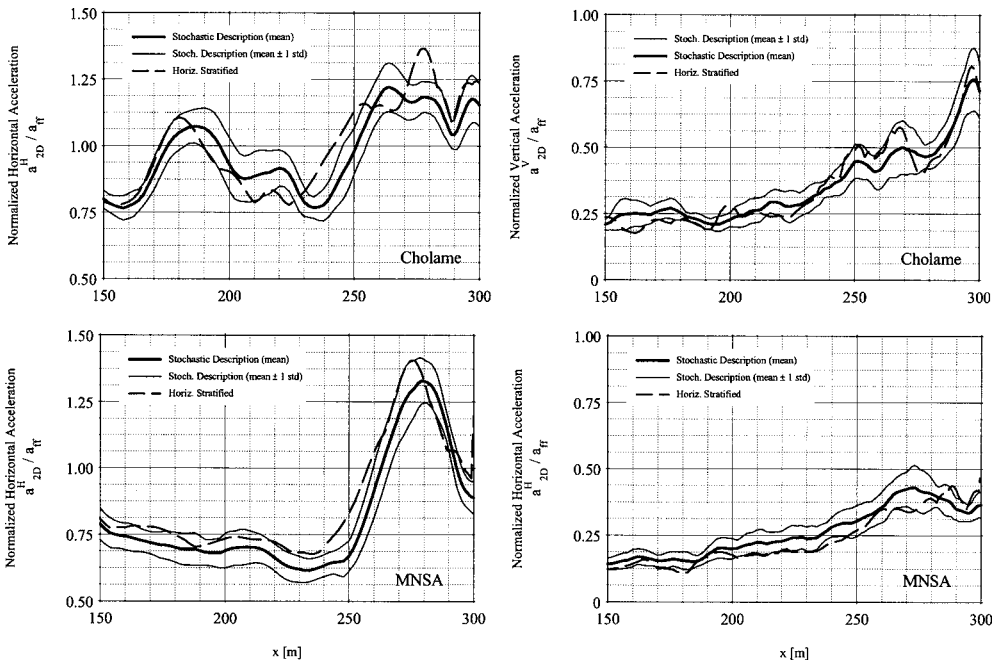

Figure 16a. Distribution of the normalized peak ground horizontal (left) and vertical parasitic (right) acceleration along the free surface behind the crest for the background medium (profile C = dashed line) and ensemble of stochastic field realizations (solid line) subjected to the Cholame and MNSA rock-outcrop motions (2-D nonlinear simulations). The light solid lines correspond to 1 standard deviation of the statistical results ($\mu \pm 1\sigma$).

Figure 16a illustrates the peak normalized nonlinear surface response for profile C and the Cholame and MNSA input motions in terms of the mean and standard deviation of the spatial distribution. For comparison, the response computed for the horizontally stratified soil profile (the background stiffness of the corresponding stochastic field) is also plotted. Figure 16b shows the transfer function surface of horizontal ground motion with respect to the far-field soil column response, for the horizontally stratified medium and a typical realization of the stochastic field. Note that the divergence between the transfer function surfaces computed for each input motion is primarily attributed to the variability in the nonlinear response of the material and the corresponding strain-compatible material properties.

In the frequency domain, individual realizations showed the effects of material heterogeneity to vary as a function of the frequency-content of seismic input motion as well as the stiffness variation of the background medium. In each case, variability arises simultaneously from the material (independent of the input motion) and strain-compatible heterogeneity (function of the excitation characteristics). In particular for the illustrated example (Figure 16b):

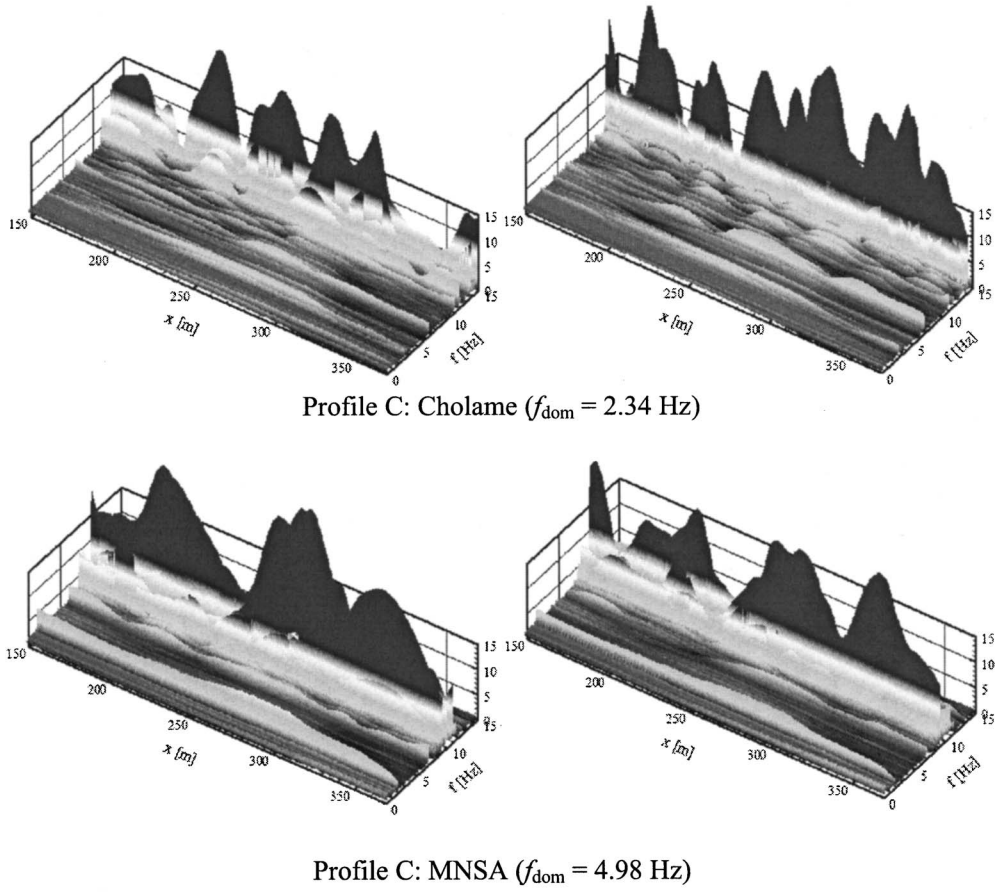

Figure 16b. Transfer function surface of horizontal acceleration (Fourier spectral ratio of surface acceleration behind the crest to the far-field surface horizontal response): comparison of response for typical realization of stochastic field (left) with the corresponding response computed for the horizontally stratified configuration of profile C (right).

- For Cholame, with dominant frequency almost coinciding with the fundamental frequency of the far field, and dominant wavelength substantially longer than the horizontal correlation distance of the stochastic field, soil heterogeneity does not reduce energy focusing at the vertex; significant enhancement of the high-frequency components is observed, a fact that implies that once the diffracted wavefield reaches the crest, short wavelengths are trapped between localized material heterogeneities and further amplified.
- For MNSA, with relatively high-frequency content compared to the fundamental frequency of profile C in the far field, the energy propagating towards the crest is

diffused by the stochastic medium.[3] As a result, the spectral amplitude of the surface ground motion is reduced, when compared to the corresponding amplitude computed for the background medium.

On the other hand, the ensemble of our simulations did not show considerable statistical difference between the spatial distribution of peak horizontal and vertical acceleration, computed using each the horizontally stratified and corresponding heterogeneous configurations (Figure 16a).

For a medium with no ground surface topographic irregularities, Assimaki et al. (2003) have illustrated that material strain softening due to strong motion is prominent in the vertical direction. As a result, small fluctuations of the stochastic field are overshadowed, rendering the horizontally stratified configuration adequate for 1-D seismic response analyses. For the Kifissos River canyon, however, localization of material yielding is controlled by a far more complex wavefield that comprises both diffracted and by direct waves, and does not ensure adequacy of the horizontally stratified configuration to compute the nonlinear 2-D response of the heterogeneous medium. It should be noted, however, that in the absence of sensitivity analyses to complement our results by investigating the effects of stiffness contrast and correlation distance of the stochastic realizations, no general conclusions could be drawn at this point.

CONCLUSIONS

Based on a case study from the 1999 Athens earthquake, we have illustrated the decisive role of local soil conditions and nonlinear soil behavior in the degree of topographic motion aggravation. We have shown the following:

- One-dimensional nonlinear soil amplification effects of seismic motion can be as high as 60% in some frequency bands, even for typical stiff sites such as the soil profiles in Adàmes, which are characterized by average shear-wave velocity $\bar{V}_s = 400\text{m/s}$ (Figure 10b).
- Topographic *aggravation* of seismic motion is a function of local soil conditions and seismic motion intensity. As a result, elastic theoretical/numerical simulations and weak motion data may not be applicable to describe topography effects for strong seismic events, especially the amplitude of high frequency components (Figure 14b).
- The equivalent-linear method with frequency-dependent dynamic soil properties may be used to describe soil amplification for horizontally stratified media, even for the case of weakly heterogeneous formations. Nonetheless, it cannot simulate the 2-D wavefield direction, and therefore cannot be used to describe the surface response of 2-D topographic features to strong ground motion, in terms of peak

[3] In particular, short-wavelength ground-motion components undergo additional 2-D reverberations, resulting in their delayed arrival and amplitude reduction at a given ground surface location. Nonetheless, this apparent amplitude reduction is attributed to energy redistribution and not to energy absorption, thus referred to as "phenomenological" attenuation.

amplitude, spatial distribution of motion, and frequency content (Figures 13a, 13b, and 14b).

- The *parasitic* acceleration component can attain quite substantial amplitude close to the crest of cliff-type topographies (on the order of magnitude of the primary far-field surface response) (Figure 13b); its amplitude is even further enhanced for the case of heterogeneous media characterized by soft surface formations and subjected to strong seismic input. Nonetheless, our simulations for vertical seismic incidence are typical of distant seismic events; further investigation is necessary to evaluate the effects of near-source events, where the incident wavefield can have a strong inclination.

Based on the common geometry of the three configurations studied, and the uniform structural density and quality reported by the Greek Ministry of Public Works within a 300-m zone parallel to the crest, the following are concluded for the effect of local soil conditions at the Kifissos ravine site:

- Profile A, the stiffest of the three sites, shows an appreciable degree of soil amplification of approximately $a_{ff}^{max} = 1.25\ a_{RO}^{max}$ (where a_{RO}^{max} is the peak amplitude of rock-outcrop motion). Topography and local soil conditions have equally contributed to the observed damage distribution at this site, and for the very stiff and relatively homogeneous profile, the moderate damage intensity can be even justified by means of elastic 2-D simulations, which predicted $a_{2D}^{hor} = 1.3\ a_{ff}^{max}$.
- Profile B is softer than profile A, and 1-D simulations show larger amplification over a wider period range (as high as $a_{ff}^{max} = 1.60\ a_{RO}^{max}$) (Figure 10b). The fundamental period of the far-field nearly coincides with the dominant period of seismic excitation, indicating the decisive role of soil conditions. This is further verified by the damage intensity distribution, nearly homogeneous within the 300-m zone behind the crest.
- Profile C is the softest of the three sites and is characterized by a rather distinct surface soil layer. One-dimensional nonlinear simulations predict no amplification (MNSA in Figure 10b) or even deamplification (Cholame in Figure 10b) of the incident seismic motion for $T < 0.25$ sec; this effect, combined with the topographic aggravation of horizontal motion ($a_{2D}^{hor} = 1.3\ a_{ff}^{max}$ in Figure 13a) cannot explain the observations for one of the most heavily damaged regions in the Athens earthquake. It is indeed the large amplitude of vertical acceleration, namely $a_{2D}^{ver} = 1.2\ a_{ff}^{max}$, which is believed to have caused substantial damage. The intensity of the parasitic motion predicted in our nonlinear simulations cannot be approximated by means of equivalent-linear analyses that yielded a marginal $a_{2D}^{ver} = 0.4\ a_{ff}^{max}$ for the same configuration.

It should be noted, however, that the site-specific conclusions were drawn: (1) using macroseismic observational evidence in the absence of strong-motion records in Adàmes during the 1999 Athens main shock to be used as input motion and quantitative validation of our nonlinear simulations, and (2) extrapolating geotechnical information and as-

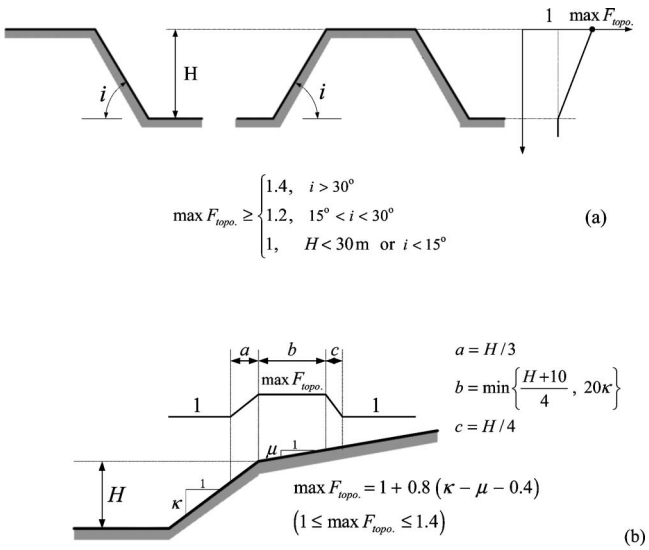

Figure 17. (a) European Seismic Code provision (*EC8*) (European Comm. 2000), and (b) French Seismic Code provision (AFPS 1990) for the aggravation factor accounting for topographic effects.

suming horizontally stratified soil configurations for the Kifissos Canyon site, due to the lack of a spatially extensive site investigation that would allow for a more detailed description of the lateral and vertical variability of soil properties.

Our study illustrates that normalizing the 2-D response by the far-field motion allows decoupling of soil and topography effects in the computed surface response. As a result, it enables the quantification of topographic motion aggravation as a function of local soil conditions, which have been well documented, extensively studied, and included in the majority of current seismic code provisions. By contrast, acquired experience on topography effects has not yet been incorporated in seismic codes, despite the volume of theoretical and numerical studies and the existence of macroseismic and instrumented evidence. Two exceptions are highlighted below:

1. The European Seismic Code (*EC8*) proposes a correction factor for both cliff and ridge type topographies, as a function of the height H and the slope inclination i (Figure 17a). Topography effects are quantified by means of a frequency-independent aggravation factor F_{topo}, defined as $a_{2-D} = F_{\text{topo}} \cdot a_{1-D}$, and are considered negligible for either $H < 30$ m or $i < 15°$.
2. The 1995 French Seismic Code (AFPS 1995) proposes a similar "aggravation" factor S_T to account for 2-D amplification on cliff-type topographies (Figure 17b), as a function of the height H of the cliff and the slope inclinations κ and μ. In this case, F_{topo} varies from 1.0 to 1.40, and the minimum slope inclination below which topographic effects are neglected is $i = 22°$.

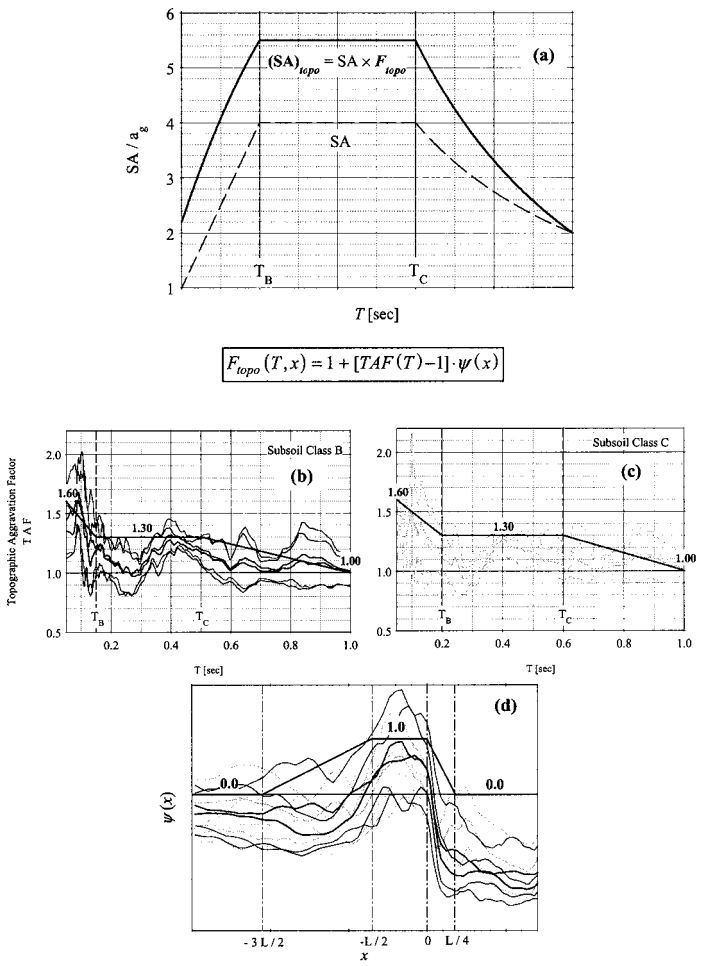

Figure 18a. Proposed design spectrum for the topographic factor, F_{topo}, which could multiply the design acceleration response spectrum of seismic code provisions to account for motion aggravation near the vertex of cliff-type topographies ($x=0$) corresponds to the vertex):

(a) Schematic illustration of typical normalized seismic code design spectrum SA(T) (accounting for local soil effects) and SA(T) $\times F_{\text{topo}}(T,x_0)$ accounting both for local soil and topography effects at location x_0).

(b) Mean and standard deviation for the ensemble of simulations (horizontally stratified and heterogeneous soil configurations and six input motions) for profiles A and B, characterized as Class B according to EC8.

(c) Same as (b) for profile C, characterized as Class C according to EC8.

(d) Spatial variation of peak horizontal normalized acceleration, as computed for all profiles and all input motions used in this study. The horizontal axis is normalized by the lateral dimension of the topographic feature ($L=70$m in this study). As shown for a cliff-type topography, $F_{\text{topo}}(T,x)$ is maximum within a zone $L/2$ behind the crest and $F_{\text{topo}}(T,x)=0$ in the far field.

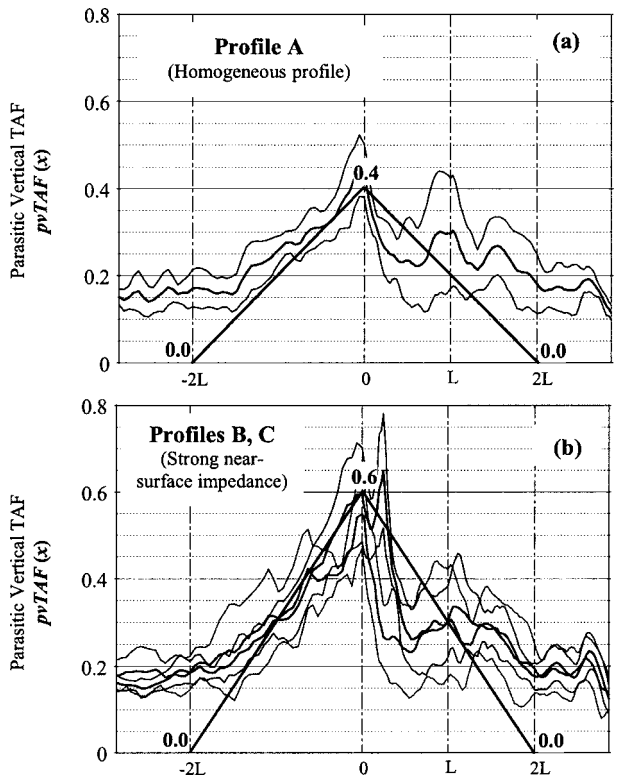

Figure 18b. Spatial distribution of the parasitic vertical Topographic Aggravation Factor (pvTAF), which will multiply the ground-motion acceleration SA(T=0) to account for the vertical acceleration component, generated close to the crest of cliff-type topographies (x=0) corresponds to the vertex) due to diffraction.

(a) Spatial variation of normalized peak vertical parasitic acceleration, computed for the ensemble of simulations for profile A. The horizontal axis is normalized by the lateral dimension of the topographic feature (L=70m in this study)

(b) Spatial variation of normalized peak vertical parasitic acceleration, computed for the ensemble of simulations for profiles B and C, both characterized by strong impedance contrast of the near-surface soil layers.

Nonetheless, case studies such as the one of Tarzana Hill in Los Angeles (Bouchon and Barker 1996) demonstrate that extremely high acceleration levels could take place (1.78 g) despite the small height (H=18m) and low slope angle (i=10°) of the configuration. Furthermore, this study also showed theoretically that such high amplification could not be theoretically predicted using a uniform soil profile with the surface topographic configuration of the site. This shows that there exist additional factors defining the lower bounds in terms of height and inclination. Furthermore, the frequency dependence of topographic aggravation, clearly illustrated in our study, needs to be explicitly addressed.

Based on the results of our simulations and those in the published literature, Figure 18a illustrates a possible scheme for a frequency- and space-dependent factor, referred to in the ensuing as *Topographic Aggravation Factor* (*TAF*). Multiplied by site-specific design spectra, the space-dependent *TAF* spectrum would provide modified spectra to account for wave diffraction and constructive interference phenomena observed, for example, at a ravine's ridge.

We believe that the high-frequency region of such a spectrum should reflect the excess enhancement of these components of motion, attributed to material heterogeneity and soil nonlinearity. Furthermore, the *TAF* spectrum should be supplemented by another design parameter, the *parasitic vertical TAF*, to account for the parasitic vertical acceleration. Normalized by the peak horizontal far-field surface response as $a_{2D}^{ver}/a_{ff}^{\max}$ (where $a_{ff}^{\max}$ corresponds to the spectral amplitude at $T=0$), the spectrum of *pvTAF* is illustrated schematically in Figure 18b as a function of distance from the crest.

Clearly, the limited number of configurations, soil conditions, and incident motions analyzed in the context of this study, not complemented by an extensive strong-motion database of case studies on topography effects, are not adequate for generalization of our conclusions for design purposes. Furthermore, considering the wide spectrum of parameters influencing the 2-D seismic response of cliff-topographies alone, a simple design rule as the one proposed here would have obvious limitations. Nonetheless, we believe that enhancing this work with additional cases studies in the years ahead, it will be possible to develop a better empirical database on the severity of the Topographic Aggravation Factor, which will allow in turn proposing the spectrum of *TAF* vis-à-vis the characteristics and dimensions of topographic features.

REFERENCES

ABAQUS, 1998. Hibbitt, Karlsson, and Sorensen, Inc., 100 Medway St., Providence, RI.

AFPS, The 1995 French Seismic Code, 1995. *Guidelines for Seismic Microzonation Studies*, October.

Aki, K., 1988. Local site effects on strong ground motion, in *Proceedings, Earthquake Engineering and Soil Dynamics* II, pp. 103–155, ASCE.

Ashford, S. A., and Sitar, N., 1997. Analysis of topographic amplification of inclined shear waves in a steep coastal bluff, *Bull. Seismol. Soc. Am.* **87**, 692–700.

Ashford, S. A., Sitar, N., Lysmer, J., and Deng, N., 1997. Topographic effects on the seismic response of steep slopes, *Bull. Seismol. Soc. Am.* **87** (3), 701–709.

Assimaki, D., 2004. Topography Effects in the 1999 Athens Earthquake: Engineering Issues in Seismology, Sc.D. thesis, Department of Civil and Environmental Engineering, MIT, Cambridge, MA.

Assimaki D., and Gazetas G., 2004. Soil and topographic amplification on canyon banks and the Athens 1999 earthquake, *J. Earthquake Eng.* **8** (1), 1–44.

Assimaki, D., and Kausel, E., 2002. An equivalent linear algorithm with frequency- and pressure-dependent moduli and damping for the seismic analysis of deep sites, *Soil Dyn. Earthquake Eng.* **22**, 959–965.

Assimaki, D., Pecker, A., Popescu, R., and Prévost, J. H., 2003. Effects of spatial variability of soil properties on surface ground motion, *J. Earthquake Eng.* **7** (1), 1–44.

Bard, P. Y., 1982. Diffracted waves and displacement field over two-dimensional elevated topographies, *Geophys. J. R. Astron. Soc.* **71**, 731–760.

Bard, P. Y., 1995. Effects of surface geology on ground motion: Some results and remaining issues, in *Proceedings, 10th European Conference on Earthquake Engineering, Vienna*, pp. 305–323.

Bard, P. Y., 1999. Local effects on strong ground motion: Physical basis and estimation methods in view of microzoning studies, in *Proceedings, Advanced Study Course on Seismotectonic and Microzonation Techniques in Earthquake Engineering* 4, Kefallinia, Greece, pp. 127–218.

Bard, P. Y., and Tucker, B. E., 1985. Ridge and tunnel effects: Comparing observations with theory, *Bull. Seismol. Soc. Am.* **75**, 905–922.

Boore, D. M., 1972. A note on the effect of simple topography on seismic SH waves, *Bull. Seismol. Soc. Am.* **62**, 275–284.

Boore, D. M., 1973. The effect of simple topography on seismic waves: Implications for accelerations recorded at Pacoima Dam, San Fernando Valley, California, *Bull. Seismol. Soc. Am.* **63**, 1603–1609.

Bouchon, M., and Barker, J. S., 1996. Seismic response of a hill: The example of Tarzana, California, *Bull. Seismol. Soc. Am.* **86**, 66–72.

Bouckovalas G. D., Kouretzis G. P., and Kalogeras I. S., 2002. Site-specific analysis of strong motion data from the September 7, 1999 Athens, Greece Earthquake, *Natural Hazards* **27** (1–2), 105–131.

Castellani, A., Chesi, C., Peano, A., and Sardella, L., 1982. Seismic response of topographic irregularities, in *Proceedings International Conference on Soil Dynamics & Earthquake Engineering*, Southampton, pp. 251–268.

Celebi, M., 1987. Topographical and geological amplification determined from strong-motion and aftershock records of the 3 March 1985 Chile Earthquake, *Bull. Seismol. Soc. Am.* **7**, 1147–1167.

Celebi, M., 1991. Topographical and geological amplification: Case studies and engineering applications, *Struct. Safety* **10**, 199–217.

Delibasis, N., Papadimitriou, P., Voulgaris, N., and Kassaras, I., 2000. The Parnitha fault: A possible relationship with other neighboring faults and causes of larger damages, *Annales Geologiques des Pays Helleniques*, 1ere Serie, T. XXXVIII, FASC. B, pp. 41–50.

European Committee for Standardization, 2000. (*EC8*) *Design Provisions for Earthquake Resistance of Structures, Part 1-1: General Rules-Seismic Actions and General Requirements for Structures*, prEN. 1998-5, Brussels.

Faccioli, E., 1991. Seismic amplification in the presence of geologic and topographic irregularities, in *Proceedings, 2nd Int. Conf. on Recent Advances in Geotechnical Earthquake Engineering and Soil Dynamics, St. Louis, Mo.*, Vol. II, pp. 1779–1797.

Finn, W. D. L., 1991. Geotechnical engineering aspects of microzonation, in *Proceedings, International Microzonation Conference, Stanford, Calif.*, Vol. 1, pp. 199–259.

Gazetas, G., 1995. The Aegion earthquake: Analysis of the causes of failure of flexible soft-story buildings, *Bulletin of the Technical Chamber of Greece*, 30–92, November.

Gazetas, G., 1996. *Soil Dynamics and Earthquake Engineering—Case Histories*, Simeon Publishers, Athens (in Greek).

Gazetas, G., Dakoulas, P., and Papageorgiou, A. S., 1990. Local soil and source mechanism

effects in the 1986 Kalamata (Greece) earthquake, *Earthquake Eng. Struct. Dyn.* **19**, 431–456.

Gazetas, G., Kallou P. V., and Psarropoulos P. N., 2002. Topography and soil effects in the M_S 5.9 Parnitha (Athens) earthquake: The case of Adámes, *Natural Hazards* **27** (1–2), 133–169.

Geli, L., Bard, P. Y., and Jullien, B., 1988. The effect of topography on earthquake ground motion. A review and new results, *Bull. Seismol. Soc. Am.* **78**, 42–63.

Hardin, B. O., and Drnevich, V. P., 1972. Shear modulus and damping in soils: Design equations and curves, *J. Soil Mech. Found. Div.* **98** (SM7), 667–692, ASCE.

Hayashi, H., Honda, M., and Yamada, T., 1992. Modeling of nonlinear stress strain relations of sands for dynamic response analysis, in *Proceedings, 3rd World Conf. on Earthquake Engineering, Madrid, Spain*, 11, Balkema, Rotterdam, pp. 6819–6825.

Imai, I., and Tonuchi, K., 1982. Correlation of N value with S-wave velocity and shear modulus, in *Proceedings, 2nd European Symposium on Penetration Testing, Amsterdam*, 1, pp. 67–72.

Kausel, E., and Assimaki, D., 2001. Simulation of dynamic, inelastic soil behavior by means of frequency-dependent shear modulus and damping, *J. Eng. Mech.* **128** (1), 34–47.

Kawase, H., and Aki, K., 1990. Topography effects at the critical SV-wave incidence: Possible explanation of damage pattern by the Whittier Narrows, California, earthquake of October 1987, *Bull. Seismol. Soc. Am.* **80**, 1–22.

Kontoes, C., Elias, P., Sykioti, O., Briole, P., Remy, D., Sachpazi, M., Veis, G., and Kotsis, I., 2000. Displacement field and fault model for the September 7, 1999 Athens earthquake inferred from ERS2 satellite radar interferometry, *Geophys. Res. Lett.* **27** (24), 3989–3992.

Leeds, D. J., 1992. Recommended accelerograms for earthquake ground motions, *USAE Waterways Experiment Station Report* **28**, S-73-1, Vicksburg, MS.

Lysmer, J., Udaka, T., Tsai, C.-F., and Seed, H. B., 1975. FLUSH—A Computer Program for Approximate 3-D Analysis of Soil-Structure Interaction Problems, *Report No. EERC 75-30*, Earthquake Engineering Research Center, University of California, Berkeley.

Papadimitriou, P., Voulgaris, N., Kassaras, I., Kaviris, G., Delibasis, N., and Makropoulos, K., 2002. The M_w=6.0, 7 September 1999 Athens Earthquake, *Natural Hazards* **27** (1–2), 15–33.

Papadopoulos, G. A., Drakatos, G., Papanastasiou, D., Kalogeras, I., and Stavrakakis, G., 2000. Preliminary results about the catastrophic earthquake of 7 September 1999 in Athens, Greece, *Seismol. Res. Lett.* **71**, 318–329.

Pavlides, S. B., Papadopoulos, G., and Ganas, A., 2002. The fault that caused the Athens September 1999 M_s=5.9 earthquake: Field observations, *Natural Hazards* **27** (1–2), 1–25.

Popescu, R., 1995. Stochastic Variability of Soil Properties: Data Analysis, Digital Simulation, Effect on System Behavior, Ph.D. dissertation, Princeton University, Princeton, NJ.

Prévost, J. H., 1995. DYNAFLOW: A nonlinear transient finite element analysis program, technical report, Dept. of Civil Eng. and Op. Research, Princeton University, Princeton, NJ.

Psycharis, I., Papastamatiou, D., Taflambas, I., Carydis, P., Bouckovalas, G., Gazetas, G., Kalogeras, I., Stavrakakis, G., Pavlides, S., Lekkas, E., Kranis, C., Ioannidis, C., Cholevas, C., and Pyrros, D., 1999. The Athens, Greece earthquake of September 7, 1999, Reconnaissance Report, EERI Newsletter Special Earthquake Report, November.

Restrepo, J. I., and Cowan, H. A., 2000. The "Eje Cafetero" earthquake, Colombia of January 25 1999, *Bull. N. Z. Natl. Soc. Earthquake Eng.* **33**, 1–29.

Rondogianni, T., Mettos, A., Galanakis, D., and Georgiou, C., 2000. The Athens earthquake of September 7, 1999: Its setting and effects, *Annales Geologiques des Pays Helleniques*, 1ere Serie, T. XXXVIII, FASC. B, pp. 131–144.

Sanchez-Sesma, F. J., 1985. Diffraction of elastic SH waves by wedges, *Bull. Seismol. Soc. Am.* **75**, 1435–1446.

Sanchez-Sesma, F., 1999. Modeling the seismic response of topographies and alluvial basins using boundary elements: Some strategies to deal with large, realistic problems, in *Proceedings, Workshop on Seismic Effects in Deep Soil Borings, Boston, Mass., March 19*.

Sanchez-Sesma, F., and Campillo, M., 1991. Diffraction of P, SV and Rayleigh waves by topographic features: A boundary integral formulation, *Bull. Seismol. Soc. Am.* **81** (6), 2234–3353.

Schnabel, P. B., Lysmer, J., and Seed, H. B., 1972. SHAKE: A computer program for earthquake response analysis of horizontally layered sites, *Report No. UCB/EERC-72/12*, Earthquake Engineering Research Center, University of California, Berkeley, December, 102 pp.

Shakal, A. M., Huang, R., Darragh, T., Cao, R., Sherburne, P., Malhotra, C., Cramer, R., Sydnor, V., Graizer, G., Maldonado, C., and Wampole, J., 1994. CSMIP strong motion records from the Northridge, California, earthquake of 17 January 1994, *Report OSMS 94-07*, California Division of Mines and Geology, Sacramento, CA.

Shinozuka, M., and Deodatis, G., 1996. Simulation of multi-dimensional Gaussian stochastic fields by spectral representation, *Appl. Mech. Rev.* **49** (1), 29–53.

Stavrakakis, G., 1999. The Athens earthquake of September 7, 1999, *Newsletter of the European Centre on Prevention and Forecasting of Earthquakes* **3**, 26–29.

Tselentis, G. A., and Zahrandnik, J., 2000. Aftershock monitoring of the Athens earthquake of 7 September 1999, *Seismol. Res. Lett.* **71** (3), 330–337.

Vucetic, M., and Dobry, R., 1991. Effect of soil plasticity on cyclic response, *J. Geotech. Eng.* **117**, 89–107.

Wong, H. L., and Trifunac, M. D., 1974. Scattering of plane SH waves by semi-elliptical canyon, *Earthquake Eng. Struct. Dyn.* **3**, 157–169.

(Received 17 March 2004; accepted 16 December 2004)